Journal of Computational Applied Mechanics 2021, 52(4): 682-716
DOI: 10.22059/jcamech.2021.323598.616

RESEARCH PAPER

The Radial Point Interpolation Method in the Bending Analysis of Symmetric Laminates Using HSDTS

D. E.S. Rodrigues [a], J. Belinha.[a, b, *], R.M. Natal Jorge [a, c]

[a] *Institute of Science and Innovation in Mechanical and Industrial Engineering, Dr. Roberto Frias Str., 400, S/N, 4200-465 Porto – Portugal.*
[b] *School of Engineering, Polytechnic of Porto (ISEP), Department of Mechanical Engineering, Rua Dr. António Bernardino de Almeida, 431, 4200-072, Porto, Portugal.*
[c] *Faculty of Engineering, University of Porto (FEUP), Department of Mechanical Engineering, Dr. Roberto Frias Str., S/N, 4200-465 Porto – Portugal.*

Abstract

The bending analysis of composite structures is usually performed using the Finite Element Method (FEM), which is also used in many fields of engineering. However, other efficient, accurate, and robust numerical methods can be alternatives to FEM's widespread use. This work focus on a meshless discretization technique - the Radial Point Interpolation Method (RPIM) – which only requires an unstructured nodal distribution to discretize the problem domain. The numerical integration of the Galerkin weak form governing the plate's bending problem is performed using a background integration mesh. The nodal connectivity is enforced using the 'influence-domain' concept which is based on a radial search of nodes closer to an integration point. Thus, in this work, the RPIM is used for the first time to analyse the bending behaviour of symmetric cross-ply composite laminated plates using equivalent single layer (ESL) formulations, following different transverse high-order shear deformation theories (HSDTs). Varying the plate's geometry and stacking sequences, the applied loads, or the plate model, several composite laminated plates are analysed. In the end, the meshless solutions are compared with analytical solutions available in the literature. The accuracy of the meshless approach is proved and several new numerical solutions for the bending of symmetric laminates are proposed.

Keywords: Symmetric Laminated Plates; High-Order Shear Deformation Theories; Meshless Method; Radial Point Interpolation Method (RPIM).

1 Introduction

Beams [1]–[4], plates and shells are key structures in engineering. The recent progress in materials' science made possible the manufacturing of these structures as advanced composite structures like laminates, sandwich panels or functionally graded [5]–[8] materials.

In the case of plates, they are three-dimensional (3D) structures but can be treated as two-dimensional (2D) solids since their thickness is much smaller than their other two dimensions. Using mostly composite laminates, the application of these structures may be found in many engineering fields, such as aircraft or aerospace components, in which it is vital to accurately predict their behaviour and avoid structural failures. To predict the mechanical behaviour of such structures, three types of 2D plate models are commonly used and frequently chosen over the classical 3D elasticity deformation theory [9], which cannot be generically applied to problems with more complex geometries. These 2D plate models are the Equivalent Single Layer (ESL) theories, the layerwise (LW) theories (which consider independent degrees of freedom for each layer resulting in accurate results but also computationally expensive) [10] and the zig-zag (ZZ)

* Corresponding Author: job@isep.ipp.pt

theories [11] (where the kinematic behaviour is described on the whole laminate, and local refinement approach acts on the scale of the layer thickness [11]). If the plate is thin, simple plate ESL theories, such as the Classical Plate Theory (CLPT) or the First-Order Shear Deformation Theory (FSDT) [12]–[15] by Reissner-Mindlin, can be used to predict, in a satisfactory way, the stress tensor installed in each point of the plate [16]. Nevertheless, the CLPT neglects the transverse shear strain and in the FSDT the distribution of the transverse shear strain is constant along with the plate's thickness, violating the traction boundary conditions at the top and bottom surface of plates [16]. Due to this last characteristic of the FSDT, shear correction factors are required in order to satisfy those conditions. Thus, the CLPT and the FSDT can only reasonably the kinematics of thin composite laminated plates [17]. Thus, for thick plates, other approaches have to be taking into account. Despite being accurate plate models, LW and ZZ theories yield solutions linked to higher computational costs when compared with other solutions proposed in the literature, such as the ESL formulation following High-order shear deformation theories (HSDTs). These theories can describe better the kinematics of a plate since they possess transverse shear functions capable to represent the nonlinear parabolic variation of transverse shear stresses through-thickness [16] and, at the same time, fulfil the traction boundary condition. The transverse shear functions used in the HSDTs can have different mathematical formulations. In the literature, it can be found transverse shear functions using polynomial [18]–[20], trigonometric [21], exponential [22],[23] or hyperbolic [24], [25] functions.

To analyse the mechanical behaviour of composite laminated plates, it is common to use numerical approaches. The finite element method (FEM) is the most used numerical tool in computational mechanics and particularly in the analysis of composite laminates. The FEM discretizes the problem domain in smaller parts called elements. Using this approach, the considered problem can be analysed in a local perspective and, subsequently, the assemblage of the elements can be performed considering their connectivity (forming the FEM's mesh). The field variable in the FEM is approximated within each element using shape functions. Unlike the FEM, in meshless methods, for instance, the concept of mesh is inexistent because these methods rely only on the position of a set of nodes discretizing the problem domain. Because there is no mathematical connection between nodes, meshless methods can handle better situations involving a transitory geometry, such as crack propagation problem, that often requires re-meshing procedures in the FEM. In meshless methods, the shape functions have virtually a higher-order, allowing a higher continuity and reproducibility [26] and the refinement procedure is simplified because nodes can be added or removed from the initial nodal mesh [27].

Meshless methods were initially proposed in 1977, with the introduction of the Smooth Particle Hydrodynamics Method (SPH) [28], being the first global weak form-based meshless method only presented in 1994 with the development of the Element Free Galerkin Method (EFGM) [29]. In these numerical methods, the field variables are approximated within an 'influence-domain' [26] which is concentric to an interest point and contains a certain number of nodes that contribute to the interpolation of the field variable at referred interest point. The overlap of 'influence-domains' assures the nodal connectivity [26], being the numerical integration performed using a background integration mesh. If the integration mesh is independent of the nodal distribution, the meshless technique is called a 'not truly' meshless method [30]. Nevertheless, this characteristic does not decrease the accuracy or efficiency of the method.

The most relevant shape functions used in meshless methods are the Taylor approximation, the moving least-square approximation, the reproducing kernel approximation, the hp-cloud approximation function, the polynomial interpolation, the parametric interpolation, the radial interpolation and the Sibson interpolation [26]. These functions need to verify the compact support property, which requires a domain of applicability and outside this domain the function assumes zero values. Concerning the type of shape functions used in the meshless methods, they can be divided into two different categories: the approximant and interpolant meshless methods. The first

ones produce smoother solutions and, because of that, the majority of meshless methods, such as the SPH and the EFGM, use approximation functions [26]. Other very popular approximant meshless methods are the Reproducing Kernel Particle Method (RKPM) [31] and the Meshless Local Petrov-Galerkin Method (MLPG) [32]. Despite the approximants meshless methods can produce smoother solutions, they do not verify a very attractive and useful numerical property: the Kronecker delta property. Field functions possessing the Kronecker delta property make simpler the numerical imposition of the essential and natural boundary conditions. Because of that, some meshless methods (such as the Point Interpolation Method (PIM) [33], the Point Assembly Method [34], the Radial Point Interpolation Method (RPIM) [35] or Natural Neighbour Radial Point Interpolation Method (NNRPIM) [26],[36]) use interpolation functions, which verify the Kronecker delta property. The RPIM is a more complex version of the PIM, using both the polynomial basis function and radial basis function (RBF), allowing the construction of stable and more robust interpolation shape functions. This is the meshless method studied in this work and it uses the Galerkin weak formulation for the definition of the discrete system of equations.

Although the FEM is the most used numerical tool to analyse composite laminated plates, several studies in the literature aim to combine distinct meshless formulations with several plate theories. For instance, the EFGM was first applied to the bending analysis of thin plates assuming the CLPT [37] and later it was formulated by Belinha *et al.* based on the FSDT for the linear and nonlinear analysis of isotropic plates and laminates [38], [39]. The Third-Order Shear Deformation Theory (TSDT) of Reddy [18] was also applied to the EFGM by Dai *et al*. [40] for static and free vibration analysis of shear deformable laminated composite plates. The RKPM was also used for the static analysis of plates and shells [41] using the FSDT. Considering several high-order shear deformation theories (developed by Levinson [42], Aydogdu [43], Karama [22] and Touratier [21]), a meshless local radial point collocation method based on multiquadric radial basis function (MQ-RBF) was proposed by Xiang *et al.* [44] for the study of the static response of isotropic, sandwich and laminated plates. The same meshless method was considered by the same authors [44] but based on inverse multiquadric RBFs for the free vibration of laminated composite plates considering the FSDT. Ferreira *et al*., in several papers, considered the FSDT [45] and the TSDT [46] [47] [17] and a global meshless approach using RBFs. The MLPG was also used in the analysis of thick laminated composite and functionally graded plates using a higher-order shear and normal deformable plate theory (HOSNDPT) [48] [49] [50]. The EFGM, RPIM, NNRPIM and NREM were recently compared in a study by Belinha *et al.* in which the authors analysed the bending behaviour of composite laminate plates using and the FSDT [27], [51].

Despite the mentioned extensive applications of meshless methods in the analysis of composite laminates, the RPIM has not been used yet in the analysis of composite laminated plates using HSDTs. In comparison with other meshless approaches, the RPIM is a rather simple numerical method whose programming simplicity resembles the FEM because the integration scheme is the same for both. Thus, the RPIM can be viewed as an advanced discretization technique that can be programmed as easily as the FEM, while having the aforementioned advantages that FEM does not have, and potentially providing smoother and more accurate results than the well-established FEM. Thus, this work focuses, for the first time in the literature, on the combination of the RPIM with bending of symmetric laminates following different HSDTs. Therefore, this work contributes with new accurate numerical solutions for this kind of analysis, expanding the range of application of meshless methods, in particular the RPIM.

2 The RPIM formulation for a 2D linear elastic problem

In the meshless methods, such as the RPIM, the nodal distribution does not form a mesh because there is no previous information regarding the spatial relationship between each node. In these numerical methods, the nodal connectivity is enforced by an overlap rule of 'influence-domains' which completely differs from the FEM formulation, where the nodal connectivity is ensured at

the element level by the interaction between nodes of adjacent elements.
In this section, the generic procedure of a meshless method is introduced. After that, the formulation of the RPIM is presented using key-concepts of the method: nodal connectivity, interpolation functions, numerical integration and the meshless discrete system of equations.

2.1 Meshless standard procedure

Most of the meshless methods, such as the RPIM, follow a standard procedure. After the description of the problem (with the essential and natural boundary conditions), the problem domain is discretized using a nodal mesh (which can be regular or irregular). Generally, irregular meshes present a lower accuracy. Nevertheless, in some problems where the locations of the stress concentration are expectable (crack propagation, holes, clamped boundaries, etc.), it is necessary to have a higher nodal density in those locations, which will lead to better results. Thus, it is essential to choose a correct nodal density for the discretization and the best nodal distribution possible (without increasing significantly the computational cost) since these discretization parameters influence the method performance. An unbalanced distribution of the nodes could lead to less accurate results [52]. After the nodal discretization, a background integration mesh is constructed. In the case of the RPIM, this integration mesh is nodal independent which ensures the characteristic of 'not truly' meshless method of the RPIM. After the definition of the integration mesh, the nodal connectivity can be imposed using the concept of 'influence-domains' [52]. The next step is to obtain the field variables, approximated within the 'influence-domains'. Consider a variable field $u(\boldsymbol{x}_\mathrm{I})$ obtained at an interest point $\boldsymbol{x}_\mathrm{I}$ within the problem domain and interpolated using the nodal values of the nodes inside the 'influence-domain' of the correspondent interest point, $\boldsymbol{x}_\mathrm{I}$. Thus, the equation of interpolation can be defined as : $u(\boldsymbol{x}_\mathrm{I}) = \sum_{\mathrm{j}=1}^{n} \varphi_j(\boldsymbol{x}_\mathrm{I}) u_j$, where n is the number of nodes within the 'influence-domain' of the interest point $\boldsymbol{x}_\mathrm{I}$, u_j is the value of the variable field in each node within the 'influence-domain' and $\varphi_j(\boldsymbol{x}_\mathrm{I})$ is the shape function of the node j obtained using only the n nodes inside the 'influence-domain' and calculated at the interest point $\boldsymbol{x}_\mathrm{I}$, [52].

After the determination of the interpolation functions, the system of equations can be arranged in a local system of discrete equations and assembled into a global system of equations. To obtain the displacement field, it can be used, for instance, the Gauss elimination method [52].

2.2 Nodal connectivity

In the RPIM, the nodal connectivity between each node is achieved with the overlap of the 'influence-domains', created following the nodal discretization and the definition of the background integration mesh. In the 2D problems analysed in this work, the 'influence-domains' for each interest point can be concentric areas with the interest point (such as circles – Figure 1 (a) – or rectangles with a predefined size). On the other hand, they can have a certain number of nodes that are closer to the interest point, as shown in Figure 1 (b). The shape and size of an 'influence-domain' may vary depending on the position of the interest points, the nodal distribution and the nodal density. For example, for a variable size 'influence-domain', it may occur that an 'influence-domain' with the same shape has a different number of nodes within it if the nodal distribution is irregular. On the opposite side, for a fixed size 'influence-domain', it is common that the shape of each domain is different. The recommendations of the literature [26] lead to the necessity of 'influence-domains' with the same number of nodes inside (for 2D problems, it is recommended between 9 and 16 nodes per 'influence-domain' [35]), which allows the construction of shape functions with the same degree of complexity.

(a) (b)

Figure 1 - (a) Fixed size 'influence-domain' ($r_I = r_J$). (b) Variable size 'influence-domain' ($r_I \neq r_J$).

2.3 Numerical integration

In the RPIM, the differential equations of the Galerkin weak form are integrated using the Gauss-Legendre quadrature. Since this work is related to the analysis of square plates, the background integration mesh is composed of quadrilateral cells (isoparametric quadrilateral shape) and in each cell are placed the Gauss integration points.

This numerical approach to solve the integro-differential equation ruling the problem does not assure the designation of a "truly" meshless method because the integration scheme neglects the nodal distribution to construct the integration mesh. Thus, the numerical integration performed in RPIM follows the same procedure as in FEM.

2.4 RPI shape functions

The RPIM uses interpolation functions based on the combination of multiquadric (MQ) radial basis functions (RBF) [35] [53] with polynomial basis functions. Consider the interpolation of $u(\boldsymbol{x}_I)$, at the integration point $\boldsymbol{x}_I$, using:

$$u(\boldsymbol{x}_I) = \boldsymbol{R}^{\mathrm{T}}(\boldsymbol{x}_I)\,\boldsymbol{a}(\boldsymbol{x}_I) + \boldsymbol{p}^{\mathrm{T}}(\boldsymbol{x}_I)\,\boldsymbol{b}(\boldsymbol{x}_I) \tag{1}$$

with,

$$\boldsymbol{R}(\boldsymbol{x}_I) = \left\{R_1(\boldsymbol{x}_I),\ R_2(\boldsymbol{x}_I),\ \ldots\ R_n(\boldsymbol{x}_I)\right\}^{\mathrm{T}} \tag{2}$$

$$\boldsymbol{p}(\boldsymbol{x}_I) = \left\{p_1(\boldsymbol{x}_I),\ p_2(\boldsymbol{x}_I),\ \ldots\ p_m(\boldsymbol{x}_I)\right\}^{\mathrm{T}} \tag{3}$$

$$\boldsymbol{a}(\boldsymbol{x}_I) = \left\{a_1(\boldsymbol{x}_I),\ a_2(\boldsymbol{x}_I),\ \ldots\ a_n(\boldsymbol{x}_I)\right\}^{\mathrm{T}} \tag{4}$$

$$\boldsymbol{b}(\boldsymbol{x}_I) = \left\{b_1(\boldsymbol{x}_I),\ b_2(\boldsymbol{x}_I),\ \ldots\ b_m(\boldsymbol{x}_I)\right\}^{\mathrm{T}} \tag{5}$$

where n is the number of nodes within the 'influence-domain' of $\boldsymbol{x}_I$, $R_i(\boldsymbol{x}_I)$ is the RBF, $a_i(\boldsymbol{x}_I)$ and $b_j(\boldsymbol{x}_I)$ are non-constant coefficients of $R_i(\boldsymbol{x}_I)$ and $p_j(\boldsymbol{x}_I)$, the polynomial basis,

respectively, with m being the basis monomial number. The RBF depends on r_{Ii}, the Euclidian distance between the interest point $\boldsymbol{x}_I$ and the neighbour node $\boldsymbol{x}_i$, given by $r_{Ii} = |\boldsymbol{x}_i - \boldsymbol{x}_I| = \sqrt{(x_I - x_i)^2 + (y_I - y_i)^2}$. The MQ-RBF used in this work is given by $R_i(\boldsymbol{x}_I) = R(r_{Ii}) = \left[r_{Ii}^2 + c^2\right]^p$, being c and p shape parameters that are considered fixed as $c = 1.42$ and $p = 1.03$, according to the literature [26].

An extra requirement needs to be satisfied if a polynomial basis function is used [26]: $\sum_{i=1}^{n} p_j(\boldsymbol{x}_i)\, a_i(\boldsymbol{x}_i) = 0 \Leftrightarrow \boldsymbol{p}^{\mathrm{T}}(\boldsymbol{x}_i)\, \boldsymbol{a}(\boldsymbol{x}_i) = 0,\ j = \{1, 2, ..., m\}$, which combined with equation (1) results in the system (6),

$$\begin{Bmatrix} \boldsymbol{u}_s \\ \boldsymbol{0} \end{Bmatrix} = \begin{bmatrix} \boldsymbol{R}(\boldsymbol{x}_I) & \boldsymbol{p}(\boldsymbol{x}_I) \\ \boldsymbol{p}^{\mathrm{T}}(\boldsymbol{x}_I) & \boldsymbol{0} \end{bmatrix} \begin{Bmatrix} \boldsymbol{a}(\boldsymbol{x}_I) \\ \boldsymbol{b}(\boldsymbol{x}_I) \end{Bmatrix} = \boldsymbol{G} \begin{Bmatrix} \boldsymbol{a}(\boldsymbol{x}_I) \\ \boldsymbol{b}(\boldsymbol{x}_I) \end{Bmatrix} \tag{6}$$

with $\boldsymbol{u}_s = \{u_1, u_2, ..., u_n\}^{\mathrm{T}}$. Matrix $\boldsymbol{R}$ has dimensions $[n \times n]$ and it is defined as $R_{ij} = R(r_{ij})$.

$$\boldsymbol{R} = \begin{bmatrix} R(r_{11}) & R(r_{12}) & \dots & R(r_{1n}) \\ R(r_{21}) & R(r_{22}) & \dots & R(r_{2n}) \\ \vdots & \vdots & \ddots & \vdots \\ R(r_{n1}) & R(r_{n2}) & \cdots & R(r_{nn}) \end{bmatrix} \tag{7}$$

The polynomial matrix, $\boldsymbol{p}$, has dimensions $[n \times m]$, being each line defined as $\boldsymbol{p}_i = \{1, x, y, x^2, xy, y^2, ...\},\ i = \{1, 2, ...n\}$ and m the chosen monomial number.

$$\boldsymbol{p} = \begin{bmatrix} \mathrm{p}_1(\boldsymbol{x}_1) & \mathrm{p}_2(\boldsymbol{x}_1) & \dots & \mathrm{p}_m(\boldsymbol{x}_1) \\ \mathrm{p}_1(\boldsymbol{x}_2) & \mathrm{p}_2(\boldsymbol{x}_2) & \dots & \mathrm{p}_m(\boldsymbol{x}_2) \\ \vdots & \vdots & \ddots & \vdots \\ \mathrm{p}_1(\boldsymbol{x}_n) & \mathrm{p}_2(\boldsymbol{x}_n) & \cdots & \mathrm{p}_m(\boldsymbol{x}_n) \end{bmatrix} \tag{8}$$

For instance, if $m = 1$, $\boldsymbol{p}$ has dimensions $[n \times 1]$ and $\boldsymbol{p}_i(\boldsymbol{x}) = \{1\}$. Matrix $\boldsymbol{G}$ in equation (6) is a symmetric matrix since the distance is directional independent. Solving equation (6) in order to the non-constant coefficients,

$$\begin{Bmatrix} \boldsymbol{a}(\boldsymbol{x}_I) \\ \boldsymbol{b}(\boldsymbol{x}_I) \end{Bmatrix} = \boldsymbol{G}^{-1} \begin{Bmatrix} \boldsymbol{u}_s \\ \boldsymbol{0} \end{Bmatrix} \tag{9}$$

and substituting (9) in (6) , the interpolation functions can finally be obtained,

$$u(\boldsymbol{x}_I) = \left\{\boldsymbol{R}^{\mathrm{T}}(\boldsymbol{x}_I),\, \boldsymbol{p}^{\mathrm{T}}(\boldsymbol{x}_I)\right\}\ \boldsymbol{G}^{-1} \begin{Bmatrix} \boldsymbol{u}_s \\ 0 \end{Bmatrix} = \boldsymbol{\varphi}(\boldsymbol{x}_I)\, \boldsymbol{u}_s \tag{10}$$

where vector $\varphi(\boldsymbol{x}_I) = \{\varphi_1(\boldsymbol{x}_I), \varphi_2(\boldsymbol{x}_I), ..., \varphi_n(\boldsymbol{x}_I)\}$ is the interpolation function calculated at the interest point $\boldsymbol{x}_I$.

2.5 Weak form and meshless discrete system of equations

In the RPIM, the discrete system of equations is obtained from the Galerkin weak form written for a generic solid with domain Ω and boundary Γ,

$$\int_{\Omega} \delta\boldsymbol{\varepsilon}^{\mathrm{T}}\boldsymbol{\sigma}\,\mathrm{d}\Omega = \int_{\Omega} \delta\boldsymbol{u}^{\mathrm{T}}\boldsymbol{b}\,\mathrm{d}\Omega + \int_{\Gamma_t} \delta\boldsymbol{u}^{\mathrm{T}}\bar{\boldsymbol{t}}\,\mathrm{d}\Gamma \tag{11}$$

being $\boldsymbol{\varepsilon}$ the strain tensor, $\boldsymbol{\sigma}$ the stress tensor, $\boldsymbol{u}$ the displacements vector, $\boldsymbol{b}$ the body forces and $\Gamma \in \Omega$ the traction boundary where the external forces $\bar{\boldsymbol{t}}$ are applied. $\delta\boldsymbol{\varepsilon}$ is the virtual strain tensor and $\delta\boldsymbol{u}$ the virtual displacement. Considering the stress-strain relation, $\boldsymbol{\sigma} = \boldsymbol{c}\,\boldsymbol{\varepsilon}$ (where $\boldsymbol{c}$ is the constitutive matrix), and the linear relation between strains and displacements, $\boldsymbol{\varepsilon} = \boldsymbol{L}\,\boldsymbol{u}$, equation (11) can be rewritten,

$$\int_{\Omega} \delta\boldsymbol{u}^{\mathrm{T}}\boldsymbol{B}^{\mathrm{T}}\,\boldsymbol{c}\,\boldsymbol{B}\,\boldsymbol{u}\,d\Omega = \int_{\Omega} \delta\boldsymbol{u}^{\mathrm{T}}\boldsymbol{H}\,\boldsymbol{b}\,d\Omega + \int_{\Gamma} \delta\boldsymbol{u}^{\mathrm{T}}\boldsymbol{H}\,\bar{\boldsymbol{t}}\,d\Gamma \tag{12}$$

where the deformation matrix, $\boldsymbol{B}$, is defined as: $\boldsymbol{B} = \sum_{j=1}^{\mathrm{n}} \boldsymbol{L}\,\varphi_j(\boldsymbol{x}_{\mathrm{I}})$, with $\boldsymbol{\varepsilon}(\boldsymbol{x}_{\mathrm{I}}) = \boldsymbol{B}\,\boldsymbol{u}$. Additionally, $\boldsymbol{H}$ represents a diagonal matrix containing the shape function component of a node j inside the 'influence-domain' of $\boldsymbol{x}_I$: $\boldsymbol{H}_j(\boldsymbol{x}_{\mathrm{I}}) = \boldsymbol{\varphi}_j(\boldsymbol{x}_{\mathrm{I}})\,\boldsymbol{I}$, being $\boldsymbol{I}$ an identity matrix with dimension $[5\times5]$. Removing the virtual displacement $\delta\boldsymbol{u}$ from equation (12), the discrete system of equations is obtained for an elasto-static problem,

$$\int_{\Omega} \boldsymbol{B}^{\mathrm{T}}\,\boldsymbol{c}\,\boldsymbol{B}\;d\Omega\;\boldsymbol{u} = \int_{\Omega} \boldsymbol{H}\,\boldsymbol{b}\,d\Omega + \int_{\Gamma} \boldsymbol{H}\,\bar{\boldsymbol{t}}\,d\Gamma \tag{13}$$

which can be written as $\boldsymbol{K}\cdot\boldsymbol{u} = \boldsymbol{F}$, with $\boldsymbol{K} = \int_{\Omega} \boldsymbol{B}^{\mathrm{T}}\,\boldsymbol{c}\,\boldsymbol{B}\;\mathrm{d}\Omega$ and $\boldsymbol{F} = \int_{\Omega} \boldsymbol{H}\,\boldsymbol{b}\,\mathrm{d}\Omega + \int_{\Gamma} \boldsymbol{H}\,\bar{\boldsymbol{t}}\,\mathrm{d}\Gamma$.

The procedure to obtain the meshless discrete system of equations is here briefly explained. A more detailed explanation can be found in the literature [26], [27], [51].

3 High-Order Shear Deformation Theories

Higher-Order Shear Deformation Theories (HSDTs) were proposed to respond to some insufficiencies of the CLPT and the FSDT. Despite being computationally more demanding, the HSDTs yield non-constant shear strains along with the plate's thickness and they fulfil the condition of zero shear stresses on the bottom and top faces of the laminated plate. In this section, the generalized displacement fields are presented as well as the transverse shear functions used in each studied HSDT. Additionally, is it presented the stress-strain relations and, in the end, the matrices of the discrete system of equations are determined.

3.1 Generalized Displacements Field and Transverse Shear Functions

The displacement field produced on a plate subjected to a generic load can be written in a generalized form considering any equivalent single layer theory. Thus, accounting five independent field variables (i.e. five generalized displacement functions of the mid surface of the plate - $u_0(x,y)$, $v_0(x,y)$, $w_0(x,y)$, $\phi_x(x,y)$ and $\phi_y(x,y)$),

$$\begin{cases} u(x,y,z) = u_0(x,y) - z\cdot\dfrac{\partial w(x,y)}{\partial x} + f(z)\cdot\left[\phi_x(x,y) + \dfrac{\partial w(x,y)}{\partial x}\right] \\ v(x,y,z) = v_0(x,y) - z\cdot\dfrac{\partial w(x,y)}{\partial y} + f(z)\cdot\left[\phi_y(x,y) + \dfrac{\partial w(x,y)}{\partial y}\right] \\ w(x,y,z) = w_0(x,y) \end{cases} \tag{14}$$

The in-plane displacements, u and v, presented in equation (14) depend on a transverse shear function, $f(z)$, which assumes a different form for each equivalent single layer theory. If $f(z)=z$, it is obtained the displacement field of the FSDT, while the equivalent is obtained for the CLPT if $f(z)=0$. The shear transverse functions are chosen such that the shear stresses assume zero values at the top and bottom surfaces of the plate (i.e. $f'(h/2)=f'(-h/2)=0$, being h the thickness of the plate).

In Figure 2 and Table 1, the transverse shear functions of the seven HSDTs studied in this work are presented. The displacement field related to each HSDT can be obtained by simply substituting the correspondent transverse shear function in equation (14).

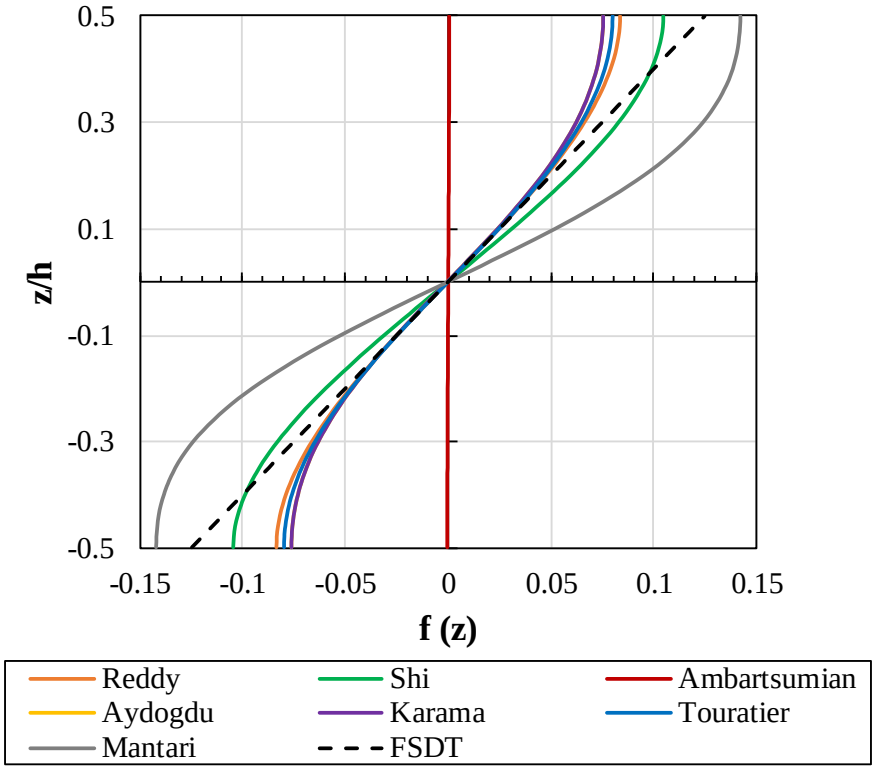

Figure 2 - Distribution of the function *f(z)* for different HSDTs along with the normalized thickness z/h.

The first three theories shown in Table 1 define the variation of the in-plane displacements along with the thickness of a plate as polynomial functions, more specifically as cubic functions. They are the third-order shear deformation theory (TSDT) of Reddy [42], [54] [18], the TSDT of Shi, [55], [56], [12] [19] and the TSDT of Ambartsumian [20]. These three TSDTs can be written in a standard form, which simplifies their computational implementation,

$$\begin{aligned}
&\text{Reddy}: f(z)=z\left(1-\frac{4z^2}{3h^2}\right)=z-\frac{4z^3}{3h^2}=k_1z+k_2z^3,\ k_1=1\wedge k_2=-\frac{4}{3h^2}\\
&\text{Shi}: f(z)=\frac{5}{4}z\left(1-\frac{4z^2}{3h^2}\right)=\frac{5}{4}z-\frac{5z^3}{3h^2}=k_1z+k_2z^3,\ k_1=\frac{5}{4}\wedge k_2=-\frac{5}{3h^2}\\
&\text{Ambartsumian}: f(z)=\frac{z}{2}\left(\frac{h^2}{4}-\frac{z^2}{3}\right)=\frac{h^2}{8}z-\frac{z^3}{6}=k_1z+k_2z^3,\ k_1=\frac{h^2}{8}\wedge k_2=-\frac{1}{6}
\end{aligned} \tag{15}$$

Table 1 - HSDTs selected for the bending analysis of composite laminated plates using the RPIM.

HSDT	$f(z)$	$f'(z)$
Levinson [42], Murthy [54] and Reddy [18]	$z\left(1-\frac{4z^2}{3h^2}\right)$	$1-\frac{4z^2}{h^2}$
Kaczkowski [55], Panc [56], Reissner [12] and Shi [19]	$\frac{5z}{4}\left(1-\frac{4z^2}{3h^2}\right)$	$\frac{5}{4}-\frac{4z^2}{h^2}$
Ambartsumian [20]	$\frac{z}{2}\left(\frac{h^2}{4}-\frac{z^2}{3}\right)$	$\frac{h^2}{8}-\frac{z^2}{2}$
Aydogdu [23]	$z\alpha^{\frac{-2\left(\frac{z}{h}\right)^2}{\ln(\alpha)}},\ \alpha=3$	$\alpha^{\frac{-2\left(\frac{z}{h}\right)^2}{\ln(\alpha)}}-4\left(\frac{z}{h}\right)^2\cdot\alpha^{\frac{-2\left(\frac{z}{h}\right)^2}{\ln(\alpha)}},\ \alpha=3$
Karama [22]	$ze^{-2\left(\frac{z}{h}\right)^2}$	$e^{-2\left(\frac{z}{h}\right)^2}-\frac{4z^2}{h^2}e^{-2\left(\frac{z}{h}\right)^2}$
Touratier [21]	$\frac{h}{\pi}\sin\left(\frac{\pi z}{h}\right)$	$\cos\left(\frac{\pi z}{h}\right)$
Mantari [58]	$\frac{h}{\pi}\left[\sin\left(\frac{\pi z}{h}\right)\cdot e^{\frac{1}{2}\cdot\cos\left(\frac{\pi z}{h}\right)}+\frac{\pi z}{2h}\right]$	$\frac{1}{2}+e^{\frac{1}{2}\cdot\cos\left(\frac{\pi z}{h}\right)}\cdot\left[\cos\left(\frac{\pi z}{h}\right)-\frac{1}{2}\cdot\text{sen}^2\left(\frac{\pi z}{h}\right)\right]$

By changing the constants k_1 and k_2 in the function $f(z)=k_1z+k_2z^3$, the transverse shear function is driven to one of the three TSDTs. If one takes a look on those constants, it can be concluded that Shi's formulation is very similar to Reddy's model because the coefficients of the linear and cubic terms are identical. On the other hand, Ambartsumian's theory has a smaller coefficient of the third-order term and, because of that, it is not expected a similar solution to the previous mentioned theories. From Figure 2**Error! Reference source not found.**, it can be seen that the distribution of Ambartsumian's transverse shear function, $f(z/h)$, is almost equal to zero $\forall\, z/h \in \left[-1/2, 1/2\right]$, which is also the case of the CLPT (where $f(z)=0$). Thus, despite being a HSDT, Ambatsumian plate theory is very similar to the CLPT, meaning that the solutions obtained from this theory, in particular for the shear stresses, will not be as accurate as the solutions obtained from the other selected HSDTs.

Another selected HSDT is the Touratier [21] model which predicts the variation of the in-plane displacements along with the thickness of the plate as a trigonometric function (it is a Trigonometric Shear Deformation Theory - TRSDT). If one takes a look on the expansions [22], [57] of the transverse shear stress function proposed by Touratier (notice that all available functions $f(z)$ that can be found in literature can be explicitly approximated in form of a unified polynomial form, as noted and studied by *Nguyen et al.* [16]),

$$\text{Touratier}: f(z)=\left(\frac{h}{\pi}\right)\sin\left(\frac{\pi z}{h}\right)=z-1.645\frac{z^3}{h^2}+0.812\frac{z^5}{h^4}-0.191\frac{z^7}{h^6}+0.0261\frac{z^9}{h^8}+... \tag{16}$$

it becomes clear that, by comparison to Reddy and Shi theories, the coefficients of the linear and cubic terms are also very similar. Nevertheless, Touratier's HSDT possesses terms with order higher than the third, which will lead to slightly higher results for the transverse shear stresses when compared with the referred TSDTs.

Karama [22] and Aydogdu [23] proposed Exponential Shear Deformation Theories (ESDT) using exponential expressions as transverse shear functions. The two models are similar, as the following expressions denote,

$$\begin{aligned}&\text{Aydogdu}: f(z)=z\alpha^{\frac{-2\left(\frac{z}{h}\right)^2}{\ln(\alpha)}}\\&\text{Karama}: f(z)=ze^{\frac{-2\left(\frac{z}{h}\right)^2}{\ln(e)}}=ze^{-2\left(\frac{z}{h}\right)^2}\end{aligned} \tag{17}$$

Karama theory is a particular case of Aydogdu's model when $\alpha=e$. This assumption allows, in computational terms, to study both ESDTs as a single one, using the dependence on α parameter. The optimal value of the parameter α was studied by Aydogdu [23]. His research concluded that assuming $\alpha=3$ leads to closer solutions to the 3D Elasticity solutions of Pagano and Hatfield [9]. Since the value of e is approximately equal to 3, Karama and Aydogdu models are not only formally similar but also mathematically equivalent. Observing the expansions of the transverse shear stress function proposed by Karama considering only the odd powers ($f(z)=ze^{-2(z/h)^2}=z-2z^3/h^2+2z^5/h^4-1.3332z^7/h^6+0.667z^9/h^8+...$) it can be concluded that, in comparison with the TRSDT of Touratier, the coefficients of successive high-order terms are decreasing more slowly, making the Karama model (proposed in 2009 [22]) stronger than the one by Touratier (dated from 1991 [21]).

Mantari [58] proposed a series of different transverse shear functions which are combinations of exponential and trigonometric functions. The theory studied on this work was proposed in 2012 and has the following generic expression,

$$\text{Mantari}: f(z)=\frac{h}{\pi}\left(\sin\left(\frac{\pi z}{h}\right)e^{m\cdot\cos\left(\frac{\pi z}{h}\right)}+\frac{\pi z}{h}m\right)\quad,\quad m\geq 0 \tag{18}$$

In the equation (18), m is a parameter optimized by Mantari in order for his theory to be closer to the 3D Elasticity solutions. Mantari proved that this situation is achieved for $m=1/2$. This considerably lowers the errors between 3D Elasticity and 2D solutions than any other existing HSDTs, according to Mantari. Notice that if $m=0$, Touratier model can be reproduced as a special case.

3.2 Stress-strain relations

The component of the strain along with the plate thickness, ε_{zz}, is considered to be zero in ESL formulations. Thus, the strain tensor written in the Voigt notation is given by $\boldsymbol{\varepsilon}=\left\{\varepsilon_{xx}\ \varepsilon_{yy}\ \gamma_{xy}\ \gamma_{yz}\ \gamma_{xz}\right\}^{\mathrm{T}}$, which can be divided in two components: the in-plane deformations, $\boldsymbol{\varepsilon}^0=\left\{\varepsilon_{xx}\ \varepsilon_{yy}\ \gamma_{xy}\right\}^{\mathrm{T}}$ and the shear components, $\boldsymbol{\gamma}=\left\{\gamma_{yz}\ \gamma_{xz}\right\}^{\mathrm{T}}$. Considering the displacement field (14) and its partial derivatives, the generalized strain field is established

$$\boldsymbol{\varepsilon}^0 = \begin{Bmatrix} \partial u/\partial x \\ \partial v/\partial y \\ \partial u/\partial y + \partial v/\partial x \end{Bmatrix} = \tag{19}$$

$$= \begin{Bmatrix} \partial u_0/\partial x \\ \partial v_0/\partial y \\ \partial u_0/\partial y + \partial v_0/\partial x \end{Bmatrix} + [f(z) - z] \cdot \begin{Bmatrix} \partial^2 w_0/\partial x^2 \\ \partial^2 w_0/\partial y^2 \\ \partial^2 w_0/\partial x \partial y \end{Bmatrix} + f(z) \cdot \begin{Bmatrix} \partial \phi_x/\partial x \\ \partial \phi_y/\partial y \\ \partial \phi_x/\partial y + \partial \phi_y/\partial x \end{Bmatrix}$$

$$\boldsymbol{\gamma} = \begin{Bmatrix} \partial u/\partial z + \partial w/\partial x \\ \partial v/\partial z + \partial w/\partial y \end{Bmatrix} = f'(z) \cdot \begin{Bmatrix} \partial w_0/\partial x + \phi_x \\ \partial w_0/\partial y + \phi_y \end{Bmatrix} \tag{20}$$

The strain field in a plate will also be different considering the different HSDTs proposed by each researcher mentioned in Table 1, and can be obtained substituting the transverse shear function and its derivative in equations (19) and (20).

Considering the compliance matrix, $\boldsymbol{s}$, which relates the strains with the stresses such that $\boldsymbol{\varepsilon} = \boldsymbol{s} \cdot \boldsymbol{\sigma}$, with $\boldsymbol{\sigma} = \{\sigma_{xx} \ \sigma_{yy} \ \tau_{xy} \ \tau_{yz} \ \tau_{zx}\}^{\mathrm{T}}$,

$$\boldsymbol{s} = \begin{bmatrix} \frac{1}{E_1} & \frac{-\nu_{21}}{E_2} & 0 & 0 & 0 \\ \frac{-\nu_{12}}{E_1} & \frac{1}{E_2} & 0 & 0 & 0 \\ 0 & 0 & \frac{1}{G_{12}} & 0 & 0 \\ 0 & 0 & 0 & \frac{1}{G_{23}} & 0 \\ 0 & 0 & 0 & 0 & \frac{1}{G_{31}} \end{bmatrix} \tag{21}$$

where, for a generic layer of a composite laminate of Figure 3, E_1 is the Young modulus along with the fibres' direction, E_2 the Young modulus along with the transverse direction, υ_{ij} is the Poisson ratio used to characterize the deformation rate in direction j when a force is applied in direction i and G_{ij} is the shear modulus characterizing the variation angle between directions i and j. Direction 3 is assumed as the cross thickness direction of the layer.

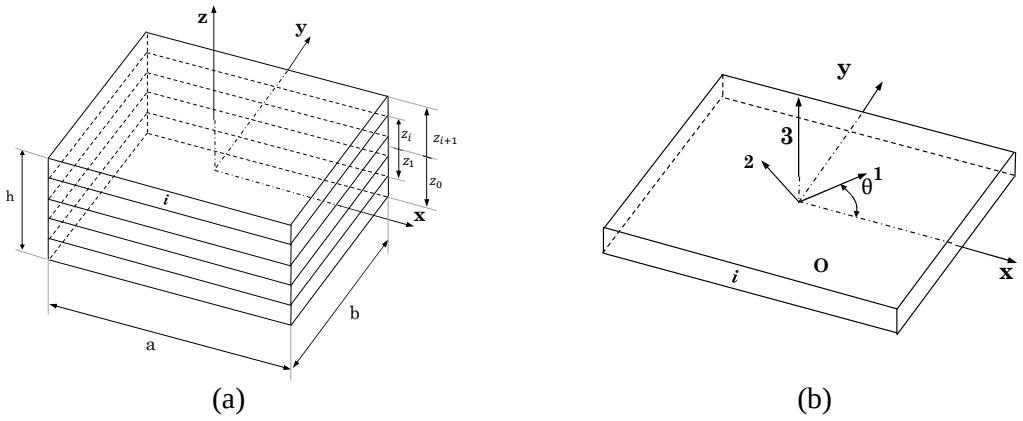

Figure 3 – (a) Composite layer distribution and correspondent global coordinate system Oxyz. (b) Local coordinate system O123.

From the compliance matrix presented in equation (21), it is possible to define the constitutive matrix, $\boldsymbol{c} = \boldsymbol{s}^{-1}$, which is defined for a local coordinate system $O123$ associated with each layer of the laminate. - Figure 3(b). This matrix needs to be transformed to the global coordinate system, applying the equation of coordinates transformation, resulting in the transformed constitutive matrix, $\boldsymbol{c}_k$,

$$\boldsymbol{c}_k = \boldsymbol{T}^T \boldsymbol{c}\, \boldsymbol{T} \tag{22}$$

where the matrix $\boldsymbol{T}$ depends on the angle of the layer, θ,

$$\boldsymbol{T} = \begin{bmatrix} \cos^2\theta & \sin^2\theta & -\sin(2\theta) & 0 & 0 \\ \sin^2\theta & \cos^2\theta & \sin(2\theta) & 0 & 0 \\ \sin\theta\cdot\cos\theta & -\sin\theta\cdot\cos\theta & \cos^2\theta-\sin^2\theta & 0 & 0 \\ 0 & 0 & 0 & \cos\theta & -\sin\theta \\ 0 & 0 & 0 & \sin\theta & \cos\theta \end{bmatrix} \tag{23}$$

The linear relation between the stress and the strain in each layer k is defined by the Hooke's law, $\boldsymbol{\sigma} = \boldsymbol{c}_k\, \boldsymbol{\varepsilon}$.

3.3 Matrix form of the discrete system of equations

To fully define the discrete system of equations represented in the equation (14), the matrices used in that equation must be determined. Since there is a different transverse shear function for each plate theory studied, the deformation matrix, $\boldsymbol{B}$, will also be different. The deformation matrix can be determined using $\boldsymbol{B}(\boldsymbol{x}_I) = \boldsymbol{L}(z)\, \boldsymbol{H}(\boldsymbol{x}_I)$, where the differential operator is a function of z and, consequentially, the deformation matrix also depends on the coordinate z. The matrix of interpolation functions has dimensions $[5 \times 5n]$ since there are five independent field variables, with n being the number of nodes within the 'influence-domain' of the interest point $\boldsymbol{x}_I$. The

differential operator can be deducted using the linear relation between strains and displacements, $\boldsymbol{\varepsilon} = \boldsymbol{L}(z)\boldsymbol{u}$, with $\boldsymbol{u} = \left\{u_0, v_0, w_0, \phi_x, \phi_y\right\}^{\mathrm{T}}$, denoted in equations (19) and (20),

$$\boldsymbol{L}(z) = \begin{bmatrix} \frac{\partial}{\partial x} & 0 & \left(f(z)-z\right)\frac{\partial^2}{\partial x^2} & f(z)\frac{\partial}{\partial x} & 0 \\ 0 & \frac{\partial}{\partial y} & \left(f(z)-z\right)\frac{\partial^2}{\partial y^2} & 0 & f(z)\frac{\partial}{\partial y} \\ \frac{\partial}{\partial y} & \frac{\partial}{\partial x} & 2\left(f(z)-z\right)\frac{\partial^2}{\partial x \partial y} & f(z)\frac{\partial}{\partial y} & f(z)\frac{\partial}{\partial x} \\ 0 & 0 & f'(z)\frac{\partial}{\partial y} & 0 & f'(z) \\ 0 & 0 & f'(z)\frac{\partial}{\partial x} & f'(z) & 0 \end{bmatrix} \tag{24}$$

For instance, using the generic transverse shear function for the TSDTs – presented in the equation (15) - the deformation matrix associated to the TSDTs selected can be defined as follows,

$$\boldsymbol{B}(\boldsymbol{x}_I) = \begin{bmatrix} \frac{\partial}{\partial x} & 0 & \left(k_1 z + k_2 z^3 - z\right)\frac{\partial^2}{\partial x^2} & \left(k_1 z + k_2 z^3\right)\frac{\partial}{\partial x} & 0 \\ 0 & \frac{\partial}{\partial y} & \left(k_1 z + k_2 z^3 - z\right)\frac{\partial^2}{\partial y^2} & 0 & \left(k_1 z + k_2 z^3\right)\frac{\partial}{\partial y} \\ \frac{\partial}{\partial y} & \frac{\partial}{\partial x} & 2\left(k_1 z + k_2 z^3 - z\right)\frac{\partial^2}{\partial x \partial y} & \left(k_1 z + k_2 z^3\right)\frac{\partial}{\partial y} & \left(k_1 z + k_2 z^3\right)\frac{\partial}{\partial x} \\ 0 & 0 & \left(k_1 + 3k_2 z^2\right)\frac{\partial}{\partial y} & 0 & \left(k_1 + 3k_2 z^2\right) \\ 0 & 0 & \left(k_1 + 3k_2 z^2\right)\frac{\partial}{\partial x} & \left(k_1 + 3k_2 z^2\right) & 0 \end{bmatrix} \boldsymbol{H}(\boldsymbol{x}_I) \tag{25}$$

which can be divided in a sum of submatrices independent of the coordinate z and affected by a distinct expressions dependent on the variable z,

$$\boldsymbol{B}(\boldsymbol{x}_I) = \boldsymbol{B}_{0M}(\boldsymbol{x}_I) + \boldsymbol{B}_{0S}(\boldsymbol{x}_I) + k_1 z \cdot \boldsymbol{B}_1(\boldsymbol{x}_I) + 3k_2 z^2 \cdot \boldsymbol{B}_2(\boldsymbol{x}_I) + k_2 z^3 \boldsymbol{B}_3(\boldsymbol{x}_I) + (k_1 z - z) \cdot \boldsymbol{B}_4(\boldsymbol{x}_I) \tag{26}$$

The deformation sub-matrices used in the equation (26) are presented by the following equations:

$$\boldsymbol{B}_{0M}^{i}(\boldsymbol{x}_I) = \begin{bmatrix} \dfrac{\partial \varphi_i(\boldsymbol{x}_I)}{\partial x} & 0 & 0 & 0 & 0 \\ 0 & \dfrac{\partial \varphi_i(\boldsymbol{x}_I)}{\partial y} & 0 & 0 & 0 \\ \dfrac{\partial \varphi_i(\boldsymbol{x}_I)}{\partial y} & \dfrac{\partial \varphi_i(\boldsymbol{x}_I)}{\partial x} & 0 & 0 & 0 \\ 0 & 0 & 0 & 0 & 0 \\ 0 & 0 & 0 & 0 & 0 \end{bmatrix} \quad i = \{1, 2, \ldots n\} \tag{27}$$

$$\boldsymbol{B}_{0S}^{i}(\boldsymbol{x}_I) = \begin{bmatrix} 0 & 0 & 0 & 0 & 0 \\ 0 & 0 & 0 & 0 & 0 \\ 0 & 0 & 0 & 0 & 0 \\ 0 & 0 & k_1 \dfrac{\partial \varphi_i(\boldsymbol{x}_I)}{\partial y} & 0 & k_1 \varphi_i(\boldsymbol{x}_I) \\ 0 & 0 & k_1 \dfrac{\partial \varphi_i(\boldsymbol{x}_I)}{\partial x} & k_1 \varphi_i(\boldsymbol{x}_I) & 0 \end{bmatrix} \quad i = \{1, 2, \ldots n\} \tag{28}$$

$$\boldsymbol{B}_{1}^{i}(\boldsymbol{x}_I) = \begin{bmatrix} 0 & 0 & 0 & \dfrac{\partial \varphi_i(\boldsymbol{x}_I)}{\partial x} & 0 \\ 0 & 0 & 0 & 0 & \dfrac{\partial \varphi_i(\boldsymbol{x}_I)}{\partial y} \\ 0 & 0 & 0 & \dfrac{\partial \varphi_i(\boldsymbol{x}_I)}{\partial y} & \dfrac{\partial \varphi_i(\boldsymbol{x}_I)}{\partial x} \\ 0 & 0 & 0 & 0 & 0 \\ 0 & 0 & 0 & 0 & 0 \end{bmatrix} \quad i = \{1, 2, \ldots n\} \tag{29}$$

$$\boldsymbol{B}_{2}^{i}(\boldsymbol{x}_I) = \begin{bmatrix} 0 & 0 & 0 & 0 & 0 \\ 0 & 0 & 0 & 0 & 0 \\ 0 & 0 & 0 & 0 & 0 \\ 0 & 0 & \dfrac{\partial \varphi_i(\boldsymbol{x}_I)}{\partial y} & 0 & \varphi_i(\boldsymbol{x}_I) \\ 0 & 0 & \dfrac{\partial \varphi_i(\boldsymbol{x}_I)}{\partial x} & \varphi_i(\boldsymbol{x}_I) & 0 \end{bmatrix} \quad i = \{1, 2, \ldots n\} \tag{30}$$

$$\boldsymbol{B}_3^i(\boldsymbol{x}_I)=\begin{bmatrix} 0 & 0 & \dfrac{\partial^2\varphi_i(\boldsymbol{x}_I)}{\partial x^2} & \dfrac{\partial\varphi_i(\boldsymbol{x}_I)}{\partial x} & 0 \\ 0 & 0 & \dfrac{\partial^2\varphi_i(\boldsymbol{x}_I)}{\partial y^2} & 0 & \dfrac{\partial\varphi_i(\boldsymbol{x}_I)}{\partial y} \\ 0 & 0 & 2\dfrac{\partial^2\varphi_i(\boldsymbol{x}_I)}{\partial x\partial y} & \dfrac{\partial\varphi_i(\boldsymbol{x}_I)}{\partial y} & \dfrac{\partial\varphi_i(\boldsymbol{x}_I)}{\partial x} \\ 0 & 0 & 0 & 0 & 0 \\ 0 & 0 & 0 & 0 & 0 \end{bmatrix} \quad i=\{1,2,\ldots n\} \tag{31}$$

$$\boldsymbol{B}_4^i(\boldsymbol{x}_I)=\begin{bmatrix} 0 & 0 & \dfrac{\partial^2\varphi_i(\boldsymbol{x}_I)}{\partial x^2} & 0 & 0 \\ 0 & 0 & \dfrac{\partial^2\varphi_i(\boldsymbol{x}_I)}{\partial y^2} & 0 & 0 \\ 0 & 0 & 2\dfrac{\partial^2\varphi_i(\boldsymbol{x}_I)}{\partial x\partial y} & 0 & 0 \\ 0 & 0 & 0 & 0 & 0 \\ 0 & 0 & 0 & 0 & 0 \end{bmatrix} \quad i=\{1,2,\ldots n\} \tag{32}$$

and,

$$\boldsymbol{B}_0(\boldsymbol{x}_I)=\boldsymbol{B}_{0M}(\boldsymbol{x}_I)+\boldsymbol{B}_{0S}(\boldsymbol{x}_I) \tag{33}$$

Using the obtained deformation matrix, the stiffness matrix can finally be obtained using the integration scheme presented in subsection 2.3.

$$\boldsymbol{K}=\int_\Omega \boldsymbol{B}^T\boldsymbol{c}\,\boldsymbol{B}\,d\Omega=\sum_{I=1}^{nQ}\widehat{\omega}_I\left(\sum_{k=1}^{n_k}\int_{z_{k-1}}^{z_k}\boldsymbol{B}^{\mathrm{T}}(\boldsymbol{x}_I)\,\boldsymbol{c}_k\,\boldsymbol{B}(\boldsymbol{x}_I)\mathrm{d}z\right) \tag{34}$$

where nQ is the number of integration points, $\widehat{\omega}_I$ is the weight of each integration point $\boldsymbol{x}_I$, n_k is the number of layers of the laminated plate, z_{k-1} and z_k are the coordinates along with the axis z (see Figure 3(a)) of bottom and top faces of the layer i and $\boldsymbol{c}_k$ is the transformed constitutive matrix of the layer i. Substituting equation (26)into equation (34), the stiffness matrix $\boldsymbol{K}$ can also be obtained considering as a sum of sub-matrices $\boldsymbol{K}_{mn}$ with $m,n=\{0,1,2,3,4\}$:

$$\boldsymbol{K}=\sum_{m=0}^{4}\sum_{n=0}^{4}\boldsymbol{K}_{mn} \tag{35}$$

being m and n the indexes of the deformation sub-matrices. The procedure to obtain the matrices $\boldsymbol{K}_{ij}=\sum_{I=1}^{nQ}\widehat{\omega}_I\cdot\sum_{k=1}^{N_k}\int_{z_{k-1}}^{z_k}\left[(z^j)\boldsymbol{B}_i^T(\boldsymbol{x}_I)\right]\cdot\boldsymbol{c}_k^i\cdot\left[(z^j)\boldsymbol{B}_j(\boldsymbol{x}_I)\right]dz$ is exemplified for $\boldsymbol{K}_{00}$ and $\boldsymbol{K}_{01}$,

$$\boldsymbol{K}_{00} = \sum_{I=1}^{nQ} \widehat{\omega}_I \cdot \sum_{k=1}^{n_k} \int_{z_{k-1}}^{z_k} \boldsymbol{B}_0^T(\boldsymbol{x}_I) \cdot \boldsymbol{c}_k \cdot \boldsymbol{B}_0(\boldsymbol{x}_I)\, \mathrm{d}z = \sum_{I=1}^{nQ} \widehat{\omega}_I \cdot \boldsymbol{B}_0^T(\boldsymbol{x}_I) \cdot \boldsymbol{c}_{00} \cdot \boldsymbol{B}_0(\boldsymbol{x}_I) \tag{36}$$

$$\boldsymbol{K}_{01} = \sum_{I=1}^{nQ} \widehat{\omega}_I \cdot \sum_{k=1}^{n_k} \int_{z_{k-1}}^{z_k} \boldsymbol{B}_0^T(\boldsymbol{x}_I) \cdot \boldsymbol{c}_k \cdot k_1 \cdot z \cdot \boldsymbol{B}_1(\boldsymbol{x}_I)\, \mathrm{d}z = \sum_{I=1}^{nQ} \widehat{\omega}_I \cdot \boldsymbol{B}_0^T(\boldsymbol{x}_I) \cdot \boldsymbol{c}_{01} \cdot \boldsymbol{B}_0(\boldsymbol{x}_I) \tag{37}$$

Where the homogenized matrix $\boldsymbol{c}_{ij}$ is obtained with $\boldsymbol{c}_{ij} = \sum_{k=1}^{N_k} \int_{z_{k-1}}^{z_k} (z^i) \cdot \boldsymbol{c}_k \cdot (z^j) dz$. Thus, matrices $\boldsymbol{c}_{00}$ and $\boldsymbol{c}_{01}$ are homogenised constitutive matrices, calculated by equations (38) and (39):

$$\boldsymbol{c}_{00} = \sum_{k=1}^{n_k} \int_{z_{k-1}}^{z_k} \boldsymbol{c}_k \, \mathrm{d}z = \sum_{k=1}^{n_k} \left(z_i - z_{i-1}\right) \cdot \boldsymbol{c}_k \tag{38}$$

$$\boldsymbol{c}_{01} = \sum_{k=1}^{n_k} \int_{z_{k-1}}^{z_k} \boldsymbol{c}_k \cdot k_1 z \, \mathrm{d}z = k_1 \cdot \sum_{k=1}^{n_k} \left(\frac{z_k^{\,2}}{2} - \frac{z_{k-1}^{\,2}}{2} \right) \cdot \boldsymbol{c}_k \tag{39}$$

The process to obtain the matrices $\boldsymbol{K}_{mn}$ uses the homogenisation of the constitutive matrices. Due to the consideration that the deformation sub-matrices do not depend on the material, they can be moved outside of the integral in equation (34). This procedure reduces the computational effort because the homogenised constitutive matrices can be separately determined and they do not depend on the integration point, $\boldsymbol{x}_I$. Following the described procedure, the other sub-matrices $\boldsymbol{K}_{mn}$ can be calculated. Changing the transverse shear function in equation (24), the stiffness matrix associated to the other selected HSDTs can be obtained.

The discrete system of equations is fully defined with the determination of the force vector, given by the sum of the vector of the body forces, $\boldsymbol{f}_b = \int_A \boldsymbol{H}(\boldsymbol{x}) \left\{ f_x \quad f_y \quad f_z \quad 0 \quad 0 \right\}^T dA$, with f_x, f_y and f_z being the body forces along x, y and z directions, respectively, and the vector of the external surface forces, $\boldsymbol{f}_e = \int_A \boldsymbol{H}(\boldsymbol{x}) \left\{ 0 \quad 0 \quad p_z \quad 0 \quad 0 \right\}^T dA$, where p_z is an external solicitation on the plate along the axis z.

4 Numerical examples

In this section are presented the obtained results for symmetric cross-ply laminates. Firstly, a convergence study is presented. Then, the solutions for the non-dimensionalized displacements and stresses are obtained for different laminates, Non-dimensionalized maximum stresses along with the thickness for various laminates are also calculated and represented in graphs for comparison purposes. Over the sub-sections, several comparisons are made, especially between the results obtained and the solutions from the literature, but also between the selected HSDTs.

4.1 Generic laminate geometry and introduction to the problem

The generic laminate geometry is presented in Figure 3(a), being a, b and h the dimensions of the composite plate, and the coordinate system has its origin at the geometrical centre of the plate. The considered material properties of each laminate layer are: $E_1 = 25$ GPa, $E_2 = 1$ GPa, $\nu_{12} = 0.25$, $G_{12} = G_{13} = 5$ GPa and $G_{23} = 2$ GPa.

The composite plates are considered to be simply supported and the loads applied are uniformly distributed transversal loads (UDL) and sinusoidally distributed transversal loads (SSL), according to equation (40), where q_0 is the nominal load,

$$q(x,y) = q_0$$
$$q(x,y) = q_0 \sin\left(\frac{\pi x}{a}\right)\sin\left(\frac{\pi y}{b}\right) \tag{40}$$

The numerical solutions obtained from the RPIM for the different HSDTs are compared, when available, with the solutions proposed by the literature. The solutions obtained for the maximum central transverse displacements and stresses are normalized considering the equations (41).

$$\bar{w} = w(\mathrm{A},z)\cdot\frac{E_2 h^3}{q_0\cdot a^4} \qquad \bar{\sigma}_{xx} = \sigma_{xx}(\mathrm{A},z)\cdot\frac{h^2}{q_0\cdot a^2} \qquad \bar{\sigma}_{yy} = \sigma_{yy}(\mathrm{A},z)\cdot\frac{h^2}{q_0\cdot a^2}$$
$$\bar{\tau}_{xy} = \tau_{xy}(\mathrm{B},z)\cdot\frac{h}{q_0\cdot a} \qquad \bar{\tau}_{yz} = \tau_{yz}(\mathrm{C},z)\cdot\frac{h}{q_0\cdot a} \qquad \bar{\tau}_{xz} = \tau_{xz}(\mathrm{D},z)\cdot\frac{h}{q_0\cdot a} \tag{41}$$

The letters A, B, C and D are points of the plane Oxy with the following coordinates: $A = \{0,0\}$, $B = \{-a/2,-b/2\}$, $C = \{0,-b/2\}$ and $D = \{a/2,0\}$. The z coordinate where the variables are calculated depends on the analysed laminated. Thus, for each composite laminate, Table 2 shows the height (measured on the z coordinate axis) where these six variables are obtained. In the mentioned Table 2, all the layers of the cross-ply laminates have the same thickness. Thus, the thickness of each layer is given by the total thickness of the plate divided by the number of layers. The only exception is the cross-ply laminate with the stacking sequence (0/90/0/90/0) where $h_1 = h_3 = h_5 = h/6$ and $h_2 = h_4 = h/4$.

Table 2 - z coordinate where the non-dimensional transverse displacement and stresses are computed.

	$\bar{w}$	$\bar{\sigma}_{xx}$	$\bar{\sigma}_{yy}$	$\bar{\tau}_{xy}$	$\bar{\tau}_{yz}$	$\bar{\tau}_{xz}$
(0/90/0)	0	h/2 (k = 3)	h/6 (k = 2)	- h/2	0 (k = 2)	0 (k = 2)
(0/90/90/0)	0	h/2 (k = 4)	h/4 (k = 3)	- h/2	0 (k = 3)	0 (k = 3)
(0/90/0/90/0)	0	h/2 (k = 5)	h/3 (k = 4)	- h/2	h/8 (k = 4)	0 (k = 3)
(0/90/90/0/90/90/0)	0	h/2 (k = 7)	5h/14 (k = 6)	- h/2	h/14 (k = 5)	0 (k = 4)

4.2 Convergence study

In order to select the discretization to be used in further analysis, a convergence study is performed. A constant polynomial basis function is used in the RPIM formulation, as suggested by the literature [51]. Regarding the 'influence-domains', in this work only fixed size 'influence-domains' are considered, obtained from a regular nodal discretization.

The limitation of the computer processor (about 18000 degrees of freedom) was not an obstacle in attempting to yield a converged solution. The highest discretization analysed is composed of 2601 nodes (corresponding to a $(50+1)\times(50+1)$ nodal mesh). In Figure 4 are presented the solutions for the maximum normalized transverse displacement of a simply supported square laminate, (0/90/90/0), subjected to a sinusoidal transverse load, and computed with seven equivalent single layer theories. The displacements are represented as a function of the number of nodes. From the convergence study presented, it can be concluded that a nodal distribution with 1089 nodes (33×33 nodal mesh) allows to achieve an acceptable converged

solution for all the studied plate theories. Despite that fact, it was observed that the Ambartsumian theory has a dissimilar way to converge when compared to the other theories. Instead of beginning with small displacements for the first step of convergence, it begins with a value near the final converged central transverse displacement. This behaviour seems to confirm the conclusion made in sub-section 3.1, where it was stated that the solutions obtained from the Ambartsumian theory are predicted to be dissimilar from the remaining HSDTs due to the shape of its transverse shear function.

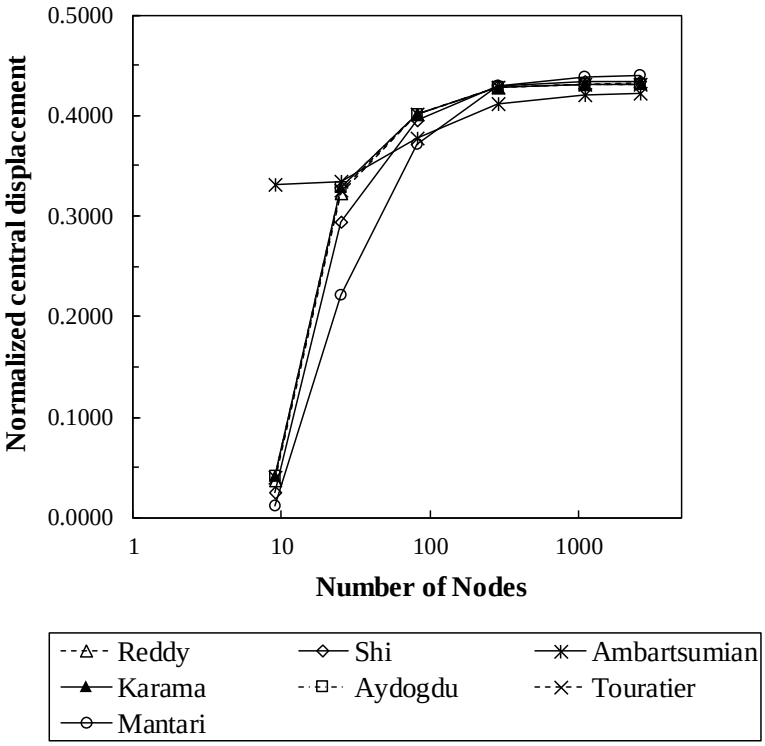

Figure 4 –Convergence study for a composite laminated square plate with the stacking sequence (0/90/90/0) square plate, with a/h=100, subjected to a sinusoidal load (SSL). Central transverse displacement as function of the number of nodes computed with RPIM.

4.3 Bending analysis of symmetric cross-ply laminates

The nodal distribution obtained from the convergence study was used for the analysis of several composite laminates with different thicknesses and subjected to two types of loads. The solutions obtained using the RPIM were computed for seven high-order shear deformation theories (Reddy, Shi, Ambartsumian, Karama, Aydogdu, Touratier and Mantari theories). The obtained results are presented from Table 3 to Table 13, where it can be found the maximum normalized displacements and stresses for symmetric cross-ply laminates with the following stacking sequences: (0/90/0), (0/90/90/0), (0/90/0/90) and (0/90/90/0/90/90/0). In those Tables are also presented, when available, the exact analytical solutions for the correspondent HSDTs as well as the 3D-Elasticity solutions. Those solutions were consulted in [23] for the Aydogdu's solutions, in [58] for Mantari and Karama's solutions, in [18] for Reddy's exact solution, in [59] for Shi's solutions and, finally, in [21] for Touratier's solutions. Ambartsumian solutions could not be found for composite laminated plates. The 3D Elasticity solutions of Pagano and Hatfield were obtained in [18].

Table 3 - Maximum normalized transverse displacements and stresses for a simply supported symmetric square laminate with cross-ply layers (0/90/0) subjected to a sinusoidal load (SSL), a/h={4,10}.

a/h	Solution	ESL	Load	$\overline{w}$	$\overline{\sigma}_{xx}$	$\overline{\sigma}_{yy}$	$\overline{\tau}_{xy}$	$\overline{\tau}_{yz}$	$\overline{\tau}_{xz}$
	Exact	Aydogdu	SSL	1.9856	0.781	0.509	0.0524	0.197	0.226
		Karama	SSL	1.944	0.775	0.502	0.0516	0.191	0.22
		Mantari	SSL	1.9434	0.823	0.497	0.0536	0.201	0.245
		Shi	SSL	1.9227	0.7337	0.5021	0.0498	0.2085	0.2856
		Touratier	SSL	-	-	-	-	-	-
		Ambartsumian	SSL	-	-	-	-	-	-
		Reddy	SSL	1.9218	0.7345	-	-	0.1832	-
4		Elasticity	SSL	2.006	0.755	0.556	0.0505	0.2172	0.282
	RPIM	Aydogdu	SSL	1.9269	0.7374	0.4734	0.0489	0.1809	0.2089
		Karama	SSL	1.9269	0.7374	0.4734	0.0489	0.1809	0.2089
		Mantari	SSL	1.9519	0.7915	0.4671	0.05	0.1874	0.233
		Shi	SSL	1.9206	0.7019	0.475	0.0481	0.1738	0.1926
		Touratier	SSL	1.9204	0.7184	0.4742	0.0482	0.1772	0.2003
		Ambartsumian	SSL	1.8537	0.6823	0.4686	0.0406	0.1666	0.1881
		Reddy	SSL	1.9097	0.6988	0.4742	0.0474	0.1733	0.192
	Exact	Aydogdu	SSL	0.7336	0.578	0.275	0.0284	0.111	0.282
		Karama	SSL	0.723	0.576	0.272	0.0281	0.108	0.272
		Mantari	SSL	0.7342	0.588	0.276	0.0288	0.115	0.314
		Shi	SSL	0.7133	0.5681	0.2687	0.0277	0.1167	0.3693
		Touratier	SSL	-	-	-	-	-	-
		Ambartsumian	SSL	-	-	-	-	-	-
		Reddy	SSL	0.7125	0.5684	-	-	0.1033	-
10		Elasticity	SSL	-	0.59	0.288	0.0289	0.1228	0.357
	RPIM	Aydogdu	SSL	0.718	0.5474	0.257	0.027	0.1026	0.2588
		Karama	SSL	0.718	0.5474	0.257	0.027	0.1026	0.2588
		Mantari	SSL	0.7409	0.5643	0.2612	0.0276	0.1077	0.3002
		Shi	SSL	0.7126	0.5414	0.2545	0.0268	0.0982	0.2331
		Touratier	SSL	0.7136	0.5434	0.2556	0.0268	0.1003	0.2452
		Ambartsumian	SSL	0.6904	0.5299	0.2524	0.0247	0.0941	0.2292
		Reddy	SSL	0.7087	0.5395	0.2541	0.0266	0.0979	0.2324

Table 4 - Maximum normalized transverse displacements and stresses for a simply supported symmetric square laminate with cross-ply layers (0/90/0) subjected to a sinusoidal load (SSL), a/h={20,100}.

a/h	Solution	ESL	Load	$\overline{w}$	$\overline{\sigma}_{xx}$	$\overline{\sigma}_{yy}$	$\overline{\tau}_{xy}$	$\overline{\tau}_{yz}$	$\overline{\tau}_{xz}$
	Exact	Aydogdu	SSL	0.511	0.548	0.206	0.0232	0.0877	0.295
		Karama	SSL	0.508	0.548	0.205	0.0231	0.086	0.285
		Mantari	SSL	0.5113	0.551	0.206	0.0233	0.09	0.331
		Shi	SSL	0.505	0.5458	0.2042	0.023	0.0919	0.3881
		Touratier	SSL	-	-	-	-	-	-
		Ambartsumian	SSL	-	-	-	-	-	-
		Reddy	SSL	-	-	-	-	-	-
20		Elasticity	SSL	-	0.552	0.21	0.0234	0.0938	0.385
	RPIM	Aydogdu	SSL	0.5038	0.5197	0.1939	0.0222	0.0815	0.2709
		Karama	SSL	0.5038	0.5197	0.1939	0.0222	0.0815	0.2709
		Mantari	SSL	0.5161	0.5282	0.196	0.0226	0.0851	0.3166
		Shi	SSL	0.5043	0.5196	0.1933	0.0223	0.0786	0.2428
		Touratier	SSL	0.5027	0.5188	0.1934	0.0222	0.0799	0.256
		Ambartsumian	SSL	0.4889	0.5094	0.1923	0.021	0.0753	0.2392
		Reddy	SSL	0.5015	0.5179	0.193	0.0222	0.0784	0.287
	Exact	Aydogdu	SSL	0.435	0.5389	0.181	0.0214	0.0791	0.3003
		Karama	SSL	0.435	0.538	0.18	0.0213	0.078	0.289
		Mantari	SSL	0.4353	0.539	0.181	0.0214	0.081	0.337
		Shi	SSL	0.4351	0.5389	0.1805	0.0214	0.0828	0.3948
		Touratier	SSL	-	-	-	-	-	-
		Ambartsumian	SSL	-	-	-	-	-	-
		Reddy	SSL	0.4342	0.539	-	-	0.075	-
100		Elasticity	SSL	0.4337	0.5384	0.1804	0.0213	0.0703	-
	RPIM	Aydogdu	SSL	0.4312	0.5105	0.1706	0.0205	0.0734	0.2753
		Karama	SSL	0.4312	0.5105	0.1706	0.0205	0.0734	0.2753
		Mantari	SSL	0.4388	0.5158	0.1717	0.0207	0.077	0.3191
		Shi	SSL	0.434	0.5124	0.171	0.0206	0.0712	0.2459
		Touratier	SSL	0.4314	0.5107	0.1706	0.0205	0.0721	0.26
		Ambartsumian	SSL	0.4209	0.5027	0.1702	0.0197	0.0755	0.2397
		Reddy	SSL	0.4317	0.5108	0.1707	0.0205	0.0709	0.2457

Table 5 - Maximum normalized transverse displacements and stresses for a simply supported symmetric rectangular (b=3a) laminate with cross-ply layers (0/90/0) subjected to a sinusoidal load (SSL).

a/h	Solution	ESL	Load	$\overline{w}$	$\overline{\sigma}_{xx}$	$\overline{\sigma}_{yy}$	$\overline{\tau}_{xy}$	$\overline{\tau}_{yz}$	$\overline{\tau}_{xz}$
	Exact	Karama	SSL	2.6838	1.0970	0.1040	0.0272	0.0360	0.2980
		Mantari	SSL	2.6841	1.1180	0.1030	0.0274	0.0360	0.3020
		Touratier	SSL	2.6660	1.0340	0.1030	0.0268	0.0355	0.2850
		Reddy	SSL	2.6410	1.0360	0.1030	0.0263	0.0348	0.2720
4		Elasticity	SSL	2.8200	1.1000	0.1190	0.0281	0.0334	0.3870
	RPIM	Karama	SSL	2.6575	1.0262	0.0959	0.0259	0.0328	0.2863
		Mantari	SSL	2.7189	1.1085	0.0994	0.0265	0.0326	0.3218
		Touratier	SSL	2.6428	0.9987	0.0957	0.0256	0.0324	0.2740
		Reddy	SSL	2.6213	0.9700	0.0952	0.0252	0.0320	0.2619
	Exact	Karama	SSL	0.8768	0.7040	0.0400	0.0117	0.0180	0.3190
		Mantari	SSL	0.8800	0.7080	0.0400	0.0118	0.0180	0.3260
		Touratier	SSL	0.8700	0.6980	0.0401	0.0116	0.0172	0.3020
		Reddy	SSL	0.8620	0.6920	0.0398	0.0115	0.0170	0.2860
10		Elasticity	SSL	0.9190	0.7250	0.0435	0.0123	0.0152	0.4200
	RPIM	Karama	SSL	0.8695	0.6571	0.0373	0.0113	0.0161	0.3071
		Mantari	SSL	0.9044	0.6817	0.0393	0.0116	0.0163	0.3581
		Touratier	SSL	0.8634	0.6518	0.0371	0.0112	0.0159	0.2906
		Reddy	SSL	0.8567	0.6465	0.0369	0.0111	0.0157	0.2752
	Exact	Karama	SSL	0.5997	0.6440	0.0290	0.0092	0.0140	0.3230
		Mantari	SSL	0.5994	0.6450	0.0290	0.0092	0.0140	0.3290
		Touratier	SSL	0.5960	0.6420	0.0290	0.0091	0.0141	0.3050
		Reddy	SSL	0.5940	0.6410	0.0289	0.0091	0.0139	0.2880
20		Elasticity	SSL	0.6100	0.6500	0.0299	0.0093	0.0119	0.4340
	RPIM	Karama	SSL	0.5930	0.6002	0.0269	0.0088	0.0133	0.3104
		Mantari	SSL	0.6114	0.6129	0.0281	0.0090	0.0134	0.3640
		Touratier	SSL	0.5916	0.5990	0.0268	0.0088	0.0131	0.2933
		Reddy	SSL	0.5901	0.5978	0.0268	0.0088	0.0130	0.2773
	Exact	Karama	SSL	0.5080	0.6200	0.0250	0.0083	0.0130	0.3230
		Mantari	SSL	0.5083	0.6240	0.0250	0.0083	0.0130	0.3310
		Touratier	SSL	0.5070	0.6240	0.0253	0.0083	0.0131	0.3060
		Reddy	SSL	0.5070	0.6240	0.0253	0.0083	0.0129	0.2890
100		Elasticity	SSL	0.5080	0.6240	0.0253	0.0083	0.0108	0.4390
	RPIM	Karama	SSL	0.5032	0.5817	0.0234	0.0080	0.0118	0.3110
		Mantari	SSL	0.5154	0.5903	0.0243	0.0081	0.0118	0.3629
		Touratier	SSL	0.5036	0.5818	0.0234	0.0080	0.0117	0.2936
		Reddy	SSL	0.5040	0.5820	0.0235	0.0080	0.0116	0.2774

Table 6 - Maximum normalized transverse displacements and stresses for a simply supported symmetric square laminate with cross-ply layers (0/90/0) subjected to a uniformly distributed load (UDL).

a/h	Solution	ESL	Load	$\overline{w}$	$\overline{\sigma}_{xx}$	$\overline{\sigma}_{yy}$	$\overline{\tau}_{xy}$	$\overline{\tau}_{yz}$	$\overline{\tau}_{xz}$
		Aydogdu	UDL	2.9242	1.0535	0.6940	0.0959	0.4179	0.3526
		Karama	UDL	2.9242	1.0535	0.6940	0.0959	0.4179	0.3526
		Mantari	UDL	2.9715	1.1385	0.6907	0.0967	0.4242	0.3876
4	RPIM	Shi	UDL	2.9065	0.9993	0.6905	0.0951	0.4069	0.3286
		Touratier	UDL	2.9098	1.0242	0.6922	0.0949	0.4122	0.3399
		Ambartsumian	UDL	2.7917	0.9667	0.6787	0.0784	0.3885	0.3198
		Reddy	UDL	2.8892	0.9948	0.6892	0.0936	0.4058	0.3275
		Aydogdu	UDL	1.0984	0.8177	0.3257	0.0528	0.3136	0.4461
		Karama	UDL	1.0984	0.8177	0.3257	0.0528	0.3136	0.4461
		Mantari	UDL	1.1335	0.8405	0.3331	0.0539	0.3267	0.5139
10	RPIM	Shi	UDL	1.0898	0.8101	0.3207	0.0525	0.3019	0.4030
		Touratier	UDL	1.0913	0.8125	0.3230	0.0524	0.3075	0.4234
		Ambartsumian	UDL	1.0536	0.7919	0.3182	0.0479	0.2916	0.3960
		Reddy	UDL	1.0836	0.8074	0.3201	0.0520	0.3011	4.0188
		Aydogdu	UDL	0.7751	0.7849	0.2235	0.0429	0.2862	0.4670
		Karama	UDL	0.7751	0.7849	0.2235	0.0429	0.2862	0.4670
		Mantari	UDL	0.7938	0.7965	0.2270	0.0436	0.3004	0.5445
20	RPIM	Shi	UDL	0.7759	0.7851	0.2224	0.0430	0.2756	0.4189
		Touratier	UDL	0.7734	0.7838	0.2228	0.0428	0.2805	0.4416
		Ambartsumian	UDL	0.7514	0.7694	0.2216	0.0404	0.2685	0.4126
		Reddy	UDL	0.7716	0.7826	0.2220	0.0427	0.2747	0.4177
		Aydogdu	UDL	0.6655	0.7732	0.1865	0.0391	0.2747	0.4739
		Karama	UDL	0.6655	0.7732	0.1865	0.0391	0.2747	0.4739
		Mantari	UDL	0.6770	0.7803	0.1883	0.0394	0.2914	0.5498
100	RPIM	Shi	UDL	0.6699	0.7759	0.1871	0.0394	0.2648	4.2310
		Touratier	UDL	0.6659	0.7734	0.1866	0.0392	0.2693	0.4475
		Ambartsumian	UDL	0.6492	0.7612	0.1868	0.0375	0.2765	4.1451
		Reddy	UDL	0.6663	0.7736	0.1867	0.0392	0.2638	0.4228

Table 7 - Maximum normalized transverse displacements and stresses for a simply supported symmetric square laminate with cross-ply layers (0/90/90/0) subjected to a sinusoidal load (SSL), a/h={4,10}.

a/h	Solution	ESL	Load	$\overline{w}$	$\overline{\sigma}_{xx}$	$\overline{\sigma}_{yy}$	$\overline{\tau}_{xy}$	$\overline{\tau}_{yz}$	$\overline{\tau}_{xz}$
4	Exact	Aydogdu	SSL	1.9590	0.7040	0.6360	0.0465	0.2600	0.2320
		Karama	SSL	1.9190	0.6690	0.6370	0.0459	0.2530	0.2260
		Mantari	SSL	1.9210	0.7400	0.6350	0.0480	0.2690	0.2540
		Shi	SSL	1.8947	0.6645	0.6316	0.0441	0.2984	0.2306
		Touratier	SSL	1.9098	0.6823	0.6342	0.0450	0.2460	0.2162
		Ambartsumian	SSL	-	-	-	-	-	-
		Reddy	SSL	1.8937	0.6651	0.6322	0.0440	0.2389	0.2064
		Elasticity	SSL	1.9540	0.7200	0.6630	0.0467	0.2920	0.2190
	RPIM	Aydogdu	SSL	1.9046	0.6662	0.6007	0.0434	0.2392	0.2146
		Karama	SSL	1.9046	0.6662	0.6007	0.0434	0.2392	0.2146
		Mantari	SSL	1.9340	0.7134	0.6017	0.0445	0.2529	0.2414
		Shi	SSL	1.8940	0.6361	0.5987	0.0426	0.2267	0.1966
		Touratier	SSL	1.8961	0.6500	0.5994	0.0428	0.2328	0.2051
		Ambartsumian	SSL	1.8264	0.6186	0.5878	0.0355	0.2195	0.1914
		Reddy	SSL	1.8828	0.6330	0.5972	0.0412	0.2262	0.1959
10	Exact	Aydogdu	SSL	0.7340	0.5520	0.3960	0.0273	0.1670	0.3030
		Karama	SSL	0.7240	0.5530	0.3930	0.0272	0.1630	0.2940
		Mantari	SSL	0.7300	0.5610	0.3950	0.0280	0.1770	0.3350
		Shi	SSL	0.7156	0.5454	0.3885	0.0268	0.1923	0.3069
		Touratier	SSL	0.7206	0.5488	0.3906	0.0270	0.1581	0.2787
		Ambartsumian	SSL	-	-	-	-	-	-
		Reddy	SSL	0.7149	0.5456	0.3888	0.0268	0.1530	0.2640
		Elasticity	SSL	0.6627	0.4989	0.3614	0.0241	0.1292	0.1670
	RPIM	Aydogdu	SSL	0.7190	0.5241	0.3709	0.0261	0.1547	0.2792
		Karama	SSL	0.7190	0.5241	0.3709	0.0261	0.1547	0.2792
		Mantari	SSL	0.7371	0.5385	0.3749	0.0266	0.1664	0.3205
		Shi	SSL	0.7150	0.5198	0.3683	0.0259	0.1454	0.2516
		Touratier	SSL	0.7155	0.5210	0.3693	0.0259	0.1498	0.2648
		Ambartsumian	SSL	0.6921	0.5085	0.3631	0.0240	0.1411	0.2469
		Reddy	SSL	0.7110	0.5179	0.3674	0.0258	0.1451	0.2508

Table 8 - Maximum normalized transverse displacements and stresses for a simply supported symmetric square laminate with cross-ply layers (0/90/90/0) subjected to a sinusoidal load (SSL), a/h={20,100}.

a/h	Solution	ESL	Load	$\overline{w}$	$\overline{\sigma}_{xx}$	$\overline{\sigma}_{yy}$	$\overline{\tau}_{xy}$	$\overline{\tau}_{yz}$	$\overline{\tau}_{xz}$
	Exact	Aydogdu	SSL	0.5120	0.5400	0.3060	0.0230	0.1340	0.3260
		Karama	SSL	0.5090	0.5410	0.3060	0.0229	0.1310	0.3160
		Mantari	SSL	0.5110	0.5430	0.3060	0.0230	0.1420	0.3620
		Shi	SSL	0.5069	0.5391	0.3054	0.0228	0.1541	0.3299
		Touratier	SSL	0.5083	0.5400	0.3048	0.0229	0.1272	0.2989
		Ambartsumian	SSL	-	-	-	-	-	-
		Reddy	SSL	0.5060	0.5393	0.3043	0.0228	0.1230	0.2825
20		Elasticity	SSL	0.5128	0.5430	0.3080	0.0230	0.1560	0.3280
	RPIM	Aydogdu	SSL	0.5053	0.5128	0.2886	0.0220	0.1243	0.3000
		Karama	SSL	0.5053	0.5128	0.2886	0.0220	0.1243	0.3000
		Mantari	SSL	0.5045	0.5122	0.2882	0.0220	0.1206	0.2839
		Shi	SSL	0.5062	0.5132	0.2882	0.0221	0.1175	0.2692
		Touratier	SSL	0.5045	0.5122	0.2882	0.0220	0.1206	0.2839
		Ambartsumian	SSL	0.4904	0.5028	0.2848	0.0209	0.1140	0.2648
		Reddy	SSL	0.5034	0.5115	0.2876	0.0220	0.1171	0.2684
	Exact	Aydogdu	SSL	0.4350	0.5380	0.2700	0.0213	0.1200	0.3360
		Karama	SSL	0.4350	0.5380	0.2700	0.0213	0.1180	0.3240
		Mantari	SSL	0.4350	0.5390	0.2710	0.0210	0.1280	0.3720
		Shi	SSL	0.4352	0.5386	0.2708	0.0214	0.1389	0.3388
		Touratier	SSL	0.4352	0.5385	0.2707	0.0213	0.1149	0.3068
		Ambartsumian	SSL	-	-	-	-	-	-
		Reddy	SSL	0.4343	0.5387	0.2708	0.0213	0.1120	0.2897
100		Elasticity	SSL	0.4337	0.5382	0.2704	0.0213	0.1008	0.1780
	RPIM	Aydogdu	SSL	0.4312	0.5102	0.2558	0.0205	0.1128	0.3081
		Karama	SSL	0.4312	0.5102	0.2558	0.0205	0.1128	0.3081
		Mantari	SSL	0.4387	0.5152	0.2574	0.0207	0.1232	0.3526
		Shi	SSL	0.4341	0.5120	0.2565	0.0206	0.1071	0.2758
		Touratier	SSL	0.4315	0.5103	0.2559	0.0205	0.1097	0.2914
		Ambartsumian	SSL	0.4206	0.5019	0.2539	0.0198	0.1143	0.2685
		Reddy	SSL	0.4317	0.5104	0.2559	0.0205	0.1067	0.2753

Table 9 - Maximum normalized transverse displacements and stresses for a simply supported symmetric square laminate with cross-ply layers (0/90/90/0) subjected to a uniformly distributed load (UDL).

a/h	Solution	ESL	Load	$\overline{w}$	$\overline{\sigma}_{xx}$	$\overline{\sigma}_{yy}$	$\overline{\tau}_{xy}$	$\overline{\tau}_{yz}$	$\overline{\tau}_{xz}$
		Aydogdu	UDL	2.8897	0.9351	0.8886	0.0865	0.4981	0.3720
		Karama	UDL	2.8897	0.9351	0.8886	0.0865	0.4981	0.3720
		Mantari	UDL	2.9411	1.0075	0.8858	0.0874	0.5188	0.4119
4	RPIM	Shi	UDL	2.8673	0.8909	0.8861	0.0854	0.4763	0.3446
		Touratier	UDL	2.8731	0.9109	0.8871	0.0853	0.4870	0.3575
		Ambartsumian	UDL	2.7516	0.8624	0.8667	0.0692	0.4577	0.3342
		Reddy	UDL	2.8496	0.8868	0.8839	0.0839	0.4753	0.3433
		Aydogdu	UDL	1.1116	0.7880	0.5232	0.0495	0.3850	0.4952
		Karama	UDL	1.1116	0.7880	0.5232	0.0495	0.3850	0.4952
		Mantari	UDL	1.1389	0.8069	0.5281	0.0506	0.4120	0.5649
10	RPIM	Shi	UDL	1.1056	0.7832	0.5192	0.0492	0.3637	0.4478
		Touratier	UDL	1.1062	0.7842	0.5209	0.0492	0.3738	0.4705
		Ambartsumian	UDL	1.0682	0.7651	0.5115	0.0451	0.3527	0.4391
		Reddy	UDL	1.0993	0.7805	0.5180	0.0488	0.3627	0.4464
		Aydogdu	UDL	0.7908	0.7861	0.3929	0.0405	0.3447	0.5325
		Karama	UDL	0.7908	0.7861	0.3929	0.0405	0.3447	0.5325
		Mantari	UDL	0.8072	0.7967	0.3960	0.0412	0.3721	0.6129
20	RPIM	Shi	UDL	0.7924	0.7872	0.3921	0.0406	0.3259	4.7834
		Touratier	UDL	0.7896	0.7854	0.3922	0.0405	0.3345	0.5042
		Ambartsumian	UDL	0.7669	0.7708	0.3876	0.0383	0.3180	0.4706
		Reddy	UDL	0.7880	0.7847	0.3913	0.0404	0.3247	0.4768
		Aydogdu	UDL	0.6791	0.7873	0.3400	0.0369	0.3304	0.5461
		Karama	UDL	0.6791	0.7873	0.3400	0.0369	0.3304	0.5461
		Mantari	UDL	0.6906	0.7944	0.3420	0.0373	0.3626	0.6250
100	RPIM	Shi	UDL	0.6837	0.7901	0.3410	0.0372	0.3127	0.4886
		Touratier	UDL	0.6796	0.7876	0.3402	0.0370	0.3207	0.5165
		Ambartsumian	UDL	0.6622	0.7744	0.3378	0.0355	0.3267	4.7735
		Reddy	UDL	0.6800	0.7878	0.3403	0.0370	0.3115	0.4879

Table 10 - Maximum normalized transverse displacements and stresses for a simply supported symmetric square laminate with cross-ply layers (0/90/0/90/0) subjected to a sinusoidal load (SSL).

a/h	Solution	ESL	Load	$\overline{w}$	$\overline{\sigma}_{xx}$	$\overline{\sigma}_{yy}$	$\overline{\tau}_{xy}$	$\overline{\tau}_{yz}$	$\overline{\tau}_{xz}$
		Aydogdu	SSL	1.5645	0.6297	0.4864	0.0322	0.2186	0.4123
		Karama	SSL	1.5645	0.6297	0.4864	0.0322	0.2145	0.4123
		Mantari	SSL	1.5324	0.6648	0.4793	0.0324	0.1939	0.4391
4	RPIM	Shi	SSL	1.5951	0.6077	0.4931	0.0321	0.2238	0.3912
		Touratier	SSL	1.5778	0.6178	0.4894	0.0320	0.2196	0.4014
		Ambartsumian	SSL	1.5409	0.5927	0.4840	0.0266	0.2169	0.3817
		Reddy	SSL	1.5858	0.6052	0.4917	0.0316	0.2232	0.3898
		Aydogdu	SSL	0.6186	0.5183	0.3827	0.0227	0.1944	0.4576
		Karama	SSL	0.6186	0.5183	0.3827	0.0227	0.1908	0.4576
		Mantari	SSL	0.6192	0.5328	0.3771	0.0229	0.1815	0.4782
10	RPIM	Shi	SSL	0.6236	0.5121	0.3879	0.0227	0.1927	0.4383
		Touratier	SSL	0.6215	0.5151	0.3855	0.0227	0.1922	0.4486
		Ambartsumian	SSL	0.6073	0.5032	0.3827	0.0213	0.1881	0.4315
		Reddy	SSL	0.6236	0.5121	0.3879	0.0227	0.1927	0.4383
		Aydogdu	SSL	0.4765	0.5112	0.3522	0.0211	0.1833	0.4739
		Karama	SSL	0.4765	0.5112	0.3522	0.0211	0.1799	0.4739
		Mantari	SSL	0.4822	0.5193	0.3521	0.0213	0.1749	0.4903
20«	RPIM	Shi	SSL	0.4811	0.5114	0.3551	0.0212	0.1799	0.4582
		Touratier	SSL	0.4776	0.5104	0.3533	0.0211	0.1801	0.4660
		Ambartsumian	SSL	0.4660	0.5011	0.3497	0.0202	0.1753	0.4500
		Reddy	SSL	0.4784	0.5097	0.3541	0.0211	0.1795	0.4565
		Aydogdu	SSL	0.4299	0.5100	0.3398	0.0205	0.1802	0.4810
		Karama	SSL	0.4299	0.5100	0.3398	0.0205	0.1769	0.4810
		Mantari	SSL	0.4371	0.5150	0.3421	0.0207	0.1763	0.4892
100	RPIM	Shi	SSL	0.4330	0.5119	0.3410	0.0206	0.1757	0.4650
		Touratier	SSL	0.4303	0.5102	0.3400	0.0205	0.1764	0.4736
		Ambartsumian	SSL	0.4193	0.5015	0.3359	0.0198	0.1833	0.4519
		Reddy	SSL	0.4306	0.5103	0.3401	0.0205	0.1753	0.4645

Table 11 - Maximum normalized transverse displacements and stresses for a simply supported symmetric square laminate with cross-ply layers (0/90/0/90/0) subjected to a uniformly distributed load (UDL).

a/h	Solution	ESL	Load	$\overline{w}$	$\overline{\sigma}_{xx}$	$\overline{\sigma}_{yy}$	$\overline{\tau}_{xy}$	$\overline{\tau}_{yz}$	$\overline{\tau}_{xz}$
		Aydogdu	UDL	2.3479	0.8921	0.6915	0.0668	0.4472	0.7283
		Karama	UDL	2.3479	0.8921	0.6915	0.0668	0.4389	0.7283
		Mantari	UDL	2.3015	0.9461	0.6646	0.0664	0.3915	0.7642
4	RPIM	Shi	UDL	2.3923	0.8591	0.7111	0.0668	0.4597	0.6984
		Touratier	UDL	2.3667	0.8740	0.7010	0.0663	0.4503	0.7128
		Ambartsumian	UDL	2.3007	0.8346	0.6961	0.0538	0.4406	0.6794
		Reddy	UDL	2.3776	0.8556	0.7091	0.0656	0.4587	0.6959
		Aydogdu	UDL	0.9585	0.7828	0.5584	0.0427	0.4344	0.8320
		Karama	UDL	0.9585	0.7828	0.5584	0.0427	0.4264	0.8320
		Mantari	UDL	0.9587	0.8036	0.5459	0.0432	0.4053	0.8635
10	RPIM	Shi	UDL	0.9721	0.7768	0.5696	0.0428	0.4307	0.8027
		Touratier	UDL	0.9632	0.7784	0.5636	0.0426	0.4292	0.8173
		Ambartsumian	UDL	0.9399	0.7597	0.5600	0.0397	0.4176	0.7875
		Reddy	UDL	0.9666	0.7742	0.5681	0.0425	0.4298	0.8000
		Aydogdu	UDL	0.7518	0.7869	0.5154	0.0377	0.4258	0.8677
		Karama	UDL	0.7518	0.7869	0.5154	0.0377	0.4179	0.8677
		Mantari	UDL	0.7605	0.7986	0.5137	0.0382	0.4074	0.8953
20	RPIM	Shi	UDL	0.7592	0.7874	0.5202	0.0380	0.4170	0.8402
		Touratier	UDL	0.7536	0.7859	0.5173	0.0377	0.4177	0.8539
		Ambartsumian	UDL	0.7348	0.7711	0.5122	0.0361	0.4067	0.8254
		Reddy	UDL	0.7550	0.7849	0.5189	0.0377	0.4159	0.8371
		Aydogdu	UDL	0.6841	0.7914	0.4971	0.0357	0.4241	0.8822
		Karama	UDL	0.6841	0.7914	0.4971	0.0357	0.4163	0.8822
		Mantari	UDL	0.6953	0.7987	0.5000	0.0361	0.4157	0.8974
100	RPIM	Shi	UDL	0.6890	0.7942	0.4988	0.0360	0.4135	0.8530
		Touratier	UDL	0.6847	0.7917	0.4974	0.0358	0.4149	0.8688
		Ambartsumian	UDL	0.6670	0.7779	0.4915	0.0345	0.4261	0.8314
		Reddy	UDL	0.6853	0.7919	0.4977	0.0358	0.4122	0.8522

Table 12 - Maximum normalized transverse displacements and stresses for a simply supported symmetric square laminate with cross-ply layers (0/90/90/0/90/90/0) subjected to a sinusoidal load (SSL).

a/h	Solution	ESL	Load	$\overline{w}$	$\overline{\sigma}_{xx}$	$\overline{\sigma}_{yy}$	$\overline{\tau}_{xy}$	$\overline{\tau}_{yz}$	$\overline{\tau}_{xz}$
		Aydogdu	SSL	1.5420	0.6195	0.5033	0.0310	0.1214	0.4066
		Karama	SSL	1.5420	0.6195	0.5033	0.0310	0.1110	0.4066
		Mantari	SSL	1.5102	0.6542	0.5038	0.0313	0.0764	0.4330
4	RPIM	Shi	SSL	1.5729	0.5980	0.5049	0.0308	0.1371	0.3860
		Touratier	SSL	1.5554	0.6078	0.5036	0.0307	0.1241	0.3959
		Ambartsumian	SSL	1.5196	0.5837	0.4951	0.0255	0.1331	0.3763
		Reddy	SSL	1.5637	0.5957	0.5033	0.0303	0.1367	0.3846
		Aydogdu	SSL	0.6123	0.5177	0.3999	0.0223	0.1033	0.4428
		Karama	SSL	0.6123	0.5177	0.3999	0.0223	0.1033	0.4428
		Mantari	SSL	0.6137	0.5331	0.3962	0.0226	0.0746	0.4614
10	RPIM	Shi	SSL	0.6206	0.5127	0.4054	0.0225	0.1238	0.4268
		Touratier	SSL	0.6151	0.5143	0.4023	0.0223	0.1137	0.4347
		Ambartsumian	SSL	0.6010	0.5022	0.3987	0.0210	0.1208	0.4185
		Reddy	SSL	0.6171	0.5110	0.4043	0.0223	0.1235	0.4254
		Aydogdu	SSL	0.4747	0.5111	0.3743	0.0210	0.1087	0.4560
		Karama	SSL	0.4642	0.5008	0.3709	0.0201	0.1149	0.4348
		Mantari	SSL	0.4807	0.5196	0.3749	0.0213	0.0733	0.4696
20	RPIM	Shi	SSL	0.4792	0.5111	0.3770	0.0211	0.1178	0.4429
		Touratier	SSL	0.4757	0.5102	0.3752	0.0210	0.1087	0.4493
		Ambartsumian	SSL	0.4642	0.5008	0.3709	0.0201	0.1149	0.4348
		Reddy	SSL	0.4765	0.5094	0.3760	0.0210	0.1175	0.4413
		Aydogdu	SSL	0.4298	0.5100	0.3640	0.0205	0.1079	0.4619
		Karama	SSL	0.4298	0.5100	0.3640	0.0205	0.0987	0.4619
		Mantari	SSL	0.4370	0.5150	0.3666	0.0207	0.0745	0.4672
100	RPIM	Shi	SSL	0.4329	0.5119	0.3653	0.0206	0.1161	0.4489
		Touratier	SSL	0.4302	0.5102	0.3642	0.0205	0.1076	0.4559
		Ambartsumian	SSL	0.4192	0.5015	0.3595	0.0198	0.1208	0.4360
		Reddy	SSL	0.4305	0.5103	0.3643	0.0205	0.1159	0.4484

As can be seen, for example in the case of the laminate (0/90/0) from Table 3 to Table 6, the solutions obtained for the non-dimensionalized transverse displacements and normal stresses computed with the RPIM are considerably close to the correspondent exact solutions, especially in Shi's theory. In the case of the shear stresses, it can be seen that they are in good agreement with each other. The percentage errors regarding the correspondent exact solutions are in most cases inferior to 7%. The RPIM shows good performance and accuracy in the elasto-static analysis of composite plates since the aforementioned conclusions are extensible to other laminates, as can be observed in the remaining Tables. Additionally, there cannot be observed numerical errors concerning the thickness of the plate when a/h=100, which shows that the RPIM is not vulnerable to the shear locking phenomenon.

Table 13 - Maximum normalized transverse displacements and stresses for a simply supported symmetric square laminate with cross-ply layers (0/90/90/0/90/90/0) subjected to a uniformly distributed load (UDL).

a/h	Solution	ESL	Load	$\overline{w}$	$\overline{\sigma}_{xx}$	$\overline{\sigma}_{yy}$	$\overline{\tau}_{xy}$	$\overline{\tau}_{yz}$	$\overline{\tau}_{xz}$
		Aydogdu	UDL	2.3146	0.8787	0.7115	0.0642	0.2421	0.7296
		Karama	UDL	2.3146	0.8787	0.7115	0.0642	0.2214	0.7296
		Mantari	UDL	2.2709	0.9331	0.6959	0.0639	0.1500	0.7658
4	RPIM	Shi	UDL	2.3584	0.8459	0.7244	0.0642	0.2749	0.6998
		Touratier	UDL	2.3330	0.8606	0.7175	0.0638	0.2483	0.7141
		Ambartsumian	UDL	2.2684	0.8224	0.7086	0.0517	0.2640	0.6802
		Reddy	UDL	2.3439	0.8425	0.7223	0.0631	0.2743	0.6972
		Aydogdu	UDL	0.9500	0.7819	0.5887	0.0418	0.2426	0.8170
		Karama	UDL	0.9500	0.7819	0.5887	0.0418	0.2219	0.8170
		Mantari	UDL	0.9517	0.8045	0.5788	0.0424	0.1599	0.8455
10	RPIM	Shi	UDL	0.9629	0.7747	0.5991	0.0420	0.2657	0.7907
		Touratier	UDL	0.9543	0.7769	0.5934	0.0418	0.2441	0.8037
		Ambartsumian	UDL	0.9309	0.7577	0.5886	0.0389	0.2580	0.7754
		Reddy	UDL	0.9574	0.7721	0.5975	0.0417	0.2652	0.7880
		Aydogdu	UDL	0.7501	0.7861	0.5556	0.0374	0.2407	0.8474
		Karama	UDL	0.7501	0.7861	0.5556	0.0374	0.2201	0.8474
		Mantari	UDL	0.7594	0.7985	0.5549	0.0379	0.1625	0.8703
20	RPIM	Shi	UDL	0.7573	0.7861	0.5603	0.0376	0.2604	0.8245
		Touratier	UDL	0.7517	0.7847	0.5573	0.0374	0.2405	0.8358
		Ambartsumian	UDL	0.7329	0.7698	0.5511	0.0357	0.2541	0.8095
		Reddy	UDL	0.7531	0.7835	0.5589	0.0374	0.2597	0.8214
		Aydogdu	UDL	0.6851	0.7903	0.5417	0.0356	0.2411	0.8601
		Karama	UDL	0.6851	0.7903	0.5417	0.0356	0.2205	0.8601
		Mantari	UDL	0.6963	0.7977	0.5451	0.0360	0.1666	0.8700
100	RPIM	Shi	UDL	0.6899	0.7932	0.5435	0.0358	0.2594	0.8359
		Touratier	UDL	0.6857	0.7906	0.5420	0.0356	0.2402	0.8491
		Ambartsumian	UDL	0.6679	0.7768	0.5350	0.0343	0.2670	0.8144
		Reddy	UDL	0.6862	0.7908	0.5422	0.0356	0.2587	0.8351

By observation of Table 14, which shows the percentage errors of the solutions presented in Table 3 and Table 4 regarding the 3D-Elasticity solutions, it can be seen the errors for the six values presented are lowered as the plate goes thinner. Nevertheless, it is established that, for thinner plates, there is no significant advantage of using HSDTs – the FSDT handles sufficiently well this kind of problem. For thicker plates, the HSDTs are needed in order to predict better the transverse shear stresses. That being stated, it can be observed in Table 14 that the shear stresses computed with Mantari's theory are the ones closer to the 3D-Elasticity solutions. This fact supports the idea of Mantari (which was referred in section 3.1) that the errors between the 3D Elasticity and the 2D solutions of Mantari are lower in the majority of the calculations than other existing high-order shear deformation theories.

Concerning the laminates (0/90/0) and (0/90/90/0), subjected to uniformly distributed loads and the laminates (0/90/0/90/0) and (0/90/90/0/90/90/0) subjected to the two considered types of load, the solutions obtained from the RPIM could not be compared with analytical solutions since they

are not available, but they are presented in this paper enhancing the state-of-the-art concerning these laminates and the used HSDTs.

In this work, the graphs of the non-dimensionalized normal and transverse shear stresses along with the thickness of a laminate were also obtained. For the simply supported square laminate with the stacking sequence (0/90/90/0), subjected to a sinusoidal load (and a/h=10), the variation of the non-dimensionalized normal and transverse shear stresses across the thickness of the laminate is represented in Figure 5. The distribution of the stresses is represented for the HSDTs in study but also for the FSDT (RPIM and exact solution). From Figure 5(a) and (b), where it is represented the distribution of the normal stresses, it can be concluded that the plots are almost indistinguishable, as expected. However, in the distribution of the transverse shear stresses, a more consistent comparison can be performed between the HSDTs and the FSDT. As seen in Figure 5(c) and (d), the FSDT predicts constant shear stresses along with the plate's thickness, violating, as expected, the traction boundary conditions. The same situation does not occur with the HSDTs, which provide more realistic distributions of the shear stresses (despite the discontinuities at the layer interface). Once again, it is Mantari's theory the one that predicts the highest shear stresses, which leads to solutions closer to the 3D-Elasticity.

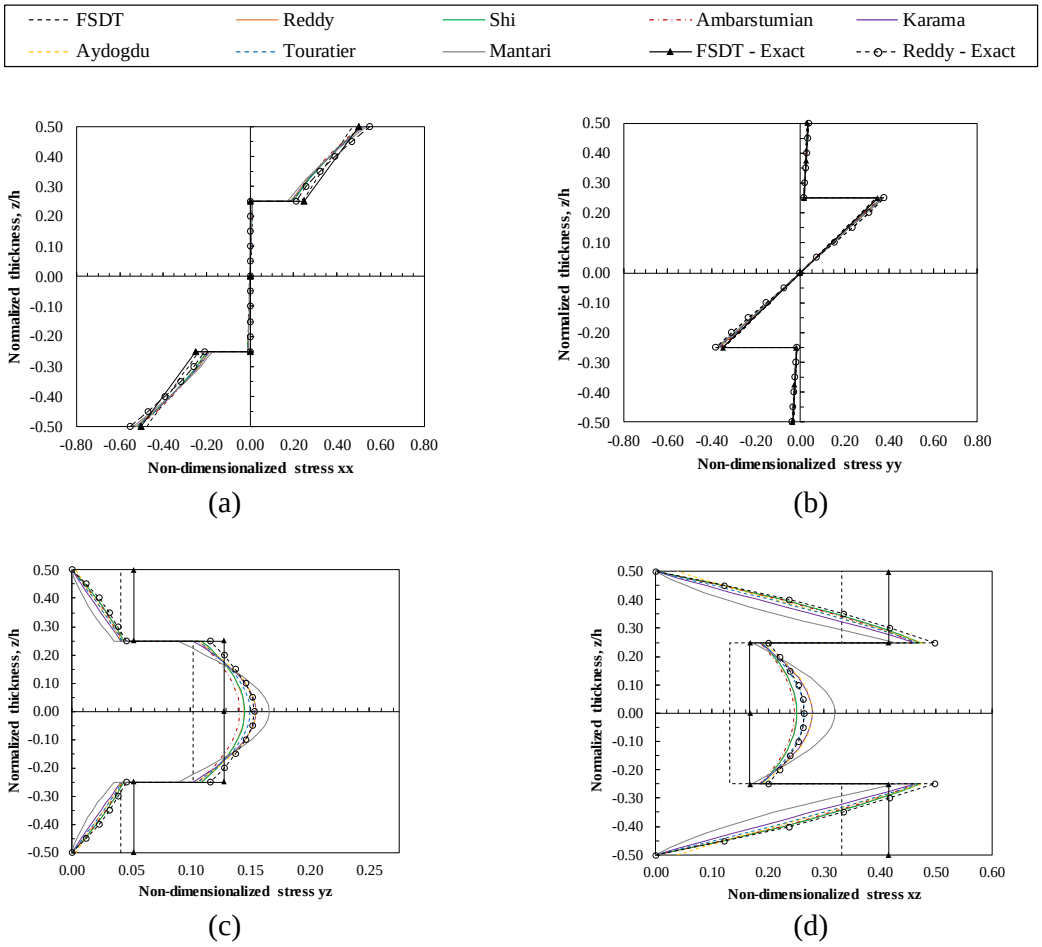

Figure 5 – Non-dimensionalized stresses for a simply supported symmetric square laminate with cross-ply layers (0/90/90/0) subjected to a sinusoidal load (SSL), a/h=4. (a) $\overline{\sigma}_{xx}$; (b) $\overline{\sigma}_{yy}$; (c) $\overline{\tau}_{yz}$; (d) $\overline{\tau}_{xz}$.

Table 14 – Relative errors (%) for the maximum normalized transverse displacements and stresses regarding the 3D-Elasticity exact solutions for a simply supported symmetric square laminate with cross-ply layers (0/90/0) subjected to a sinusoidal load (SSL).

		Relative errors (%) regarding the 3D-Elasticity exact solutions					
a/h	ESL	$\overline{w}$	$\overline{\sigma}_{xx}$	$\overline{\sigma}_{yy}$	$\overline{\tau}_{xy}$	$\overline{\tau}_{yz}$	$\overline{\tau}_{xz}$
4	Aydogdu	3.9	2.3	14.9	3.2	16.7	25.9
	Karama	3.9	2.3	14.9	3.2	16.7	25.9
	Mantari	2.7	-4.8	16.0	1.0	13.7	17.4
	Shi	4.3	7.0	14.6	4.8	20.0	31.7
	Touratier	4.3	4.8	14.7	4.6	18.4	29.0
	Ambartsumian	7.6	9.6	15.7	19.6	23.3	33.3
	Reddy	4.8	7.4	14.7	6.1	20.2	31.9
10	Aydogdu	-	7.2	10.8	6.6	16.4	27.5
	Karama	-	7.2	10.8	6.6	16.4	27.5
	Mantari	-	4.4	9.3	4.5	12.3	15.9
	Shi	-	8.2	11.6	7.3	20.0	34.7
	Touratier	-	7.9	11.3	7.3	18.3	31.3
	Ambartsumian	-	10.2	12.4	14.5	23.4	35.8
	Reddy	-	8.6	11.8	8.0	20.3	34.9
20	Aydogdu	-	5.9	7.7	5.1	13.1	29.6
	Karama	-	5.9	7.7	5.1	13.1	29.6
	Mantari	-	4.3	6.7	3.4	9.3	17.8
	Shi	-	5.9	8.0	4.7	16.2	36.9
	Touratier	-	6.0	7.9	5.1	14.8	33.5
	Ambartsumian	-	7.7	8.4	10.3	19.7	37.9
	Reddy	-	6.2	8.1	5.1	16.4	25.5
100	Aydogdu	0.6	5.2	5.4	3.8	-4.4	-
	Karama	0.6	5.2	5.4	3.8	-4.4	-
	Mantari	-1.2	4.2	4.8	2.8	-9.5	-
	Shi	-0.1	4.8	5.2	3.3	-1.3	-
	Touratier	0.5	5.1	5.4	3.8	-2.6	-
	Ambartsumian	3.0	6.6	5.7	7.5	-7.4	-
	Reddy	0.5	5.1	5.4	3.8	-0.9	-

5 Conclusions

The RPIM is used in this work for the bending analysis of symmetric cross-ply laminates. The accuracy of the RPIM is highlighted when the present solutions are compared to the correspondent exact solutions. On the other hand, the robustness is shown by the obtained linear asymptotic convergences and stable solutions. The RPIM used in this work is a 'not truly' meshless method since it uses a background nodal independent integration mesh where the Gauss-Legendre quadrature is implemented. However, being a 'not truly' meshless method does not decrease its accuracy or efficiency. In fact, because RPIM is an interpolator meshless method and uses a background lattice to build the integration mesh, it can be combined straightforwardly with the FEM, allowing hybrid FEM-meshless analyses - both methods share the same integration scheme. Since the nodal connectivity is enforced by the overlap of 'influence-domains' (which are based on radial searches), the method can be extended to more complex analyses of composite plates

such as large deformation problems or fracture mechanics. These mentioned problems are more easily analysed using the RPIM or other meshless methods since in these methods there are no mesh distortions. This later remark gives meshless methods a clear advantage over the FEM. However, despite the benefit of using meshless methods can be higher in areas where cracks or large deformations are involved, they can still be robust and accurate numerical tools (sometimes even more accurate than the FEM) in every other area covered so far by the FEM (several distinct linear-elastic solid mechanics analysis [26], [27], [60], [61] were already performed in the literature using the RPIM).

In this work, symmetric composite laminated plates were subjected to bending and the plate's in-plane displacements were approximated using different High-Order Shear Deformation Theories (HSDTs). The results presented in the work mark the first time the RPIM is used in this type of analysis. Notice RPIM was used in the past for the bending analysis of plates, but considering the first order deformation theory (FSDT) [27]. HSDTs can describe better the kinematics of a plate when compared with the FSDT because they possess transverse shear functions capable to represent the nonlinear variation of transverse shear stresses through the thickness of the plate. Thus, this work extends the field of application of the RPIM by presenting new and accurate numerical solutions that aim to enhance the state-of-the-art concerning plates' theory and computational methods, and proving the great potential of advanced discretization techniques like the RPIM.

Acknowledges

The authors truly acknowledge the funding provided by Ministério da Ciência, Tecnologia e Ensino Superior – Fundação para a Ciência e a Tecnologia (Portugal), under grant SFRH/BD/121019/2016, and by project funding MIT-EXPL/ISF/0084/2017. Additionally, the authors gratefully acknowledge the funding of Project NORTE-01-0145-FEDER-000022 – SciTech – Science and Technology for Competitive and Sustainable Industries, co-financed by Programa Operacional Regional do Norte (NORTE2020), through Fundo Europeu de Desenvolvimento Regional (FEDER).

References

[1] S. H. M. Sadek, J. Belinha, M. P. L. Parente, R. M. Natal Jorge, J. M. A. C. de Sá, and A. J. M. Ferreira, "The analysis of composite laminated beams using a 2D interpolating meshless technique," *Acta Mech. Sin.*, vol. 34, no. 1, pp. 99–116, 2018, doi: 10.1007/s10409-017-0701-8.

[2] M. M. Khoram, M. Hosseini, A. Hadi, and M. Shishehsaz, "Bending Analysis of Bidirectional FGM Timoshenko Nanobeam Subjected to Mechanical and Magnetic Forces and Resting on Winkler–Pasternak Foundation," *Int. J. Appl. Mech.*, vol. 12, no. 08, p. 2050093, Sep. 2020, doi: 10.1142/S1758825120500933.

[3] J. C. Steuben, A. P. Iliopoulos, and J. G. Michopoulos, "Discrete element modeling of particle-based additive manufacturing processes," *Comput. Methods Appl. Mech. Eng.*, vol. 305, pp. 537–561, 2016, doi: 10.1016/j.cma.2016.02.023.

[4] A. Barati, A. Hadi, M. Z. Nejad, and R. Noroozi, "On vibration of bi-directional functionally graded nanobeams under magnetic field," *Mech. Based Des. Struct. Mach.*, pp. 1–18, Feb. 2020, doi: 10.1080/15397734.2020.1719507.

[5] M. Hosseini, M. Shishesaz, and A. Hadi, "Thermoelastic analysis of rotating functionally graded micro/nanodisks of variable thickness," *Thin-Walled Struct.*, vol. 134, no. October 2018, pp. 508–523, 2019, doi: 10.1016/j.tws.2018.10.030.

[6] M. Shishesaz, M. Hosseini, K. Naderan Tahan, and A. Hadi, "Analysis of functionally graded nanodisks under thermoelastic loading based on the strain gradient theory," *Acta Mech.*, vol. 228, no. 12, pp. 4141–4168, 2017, doi: 10.1007/s00707-017-1939-8.

[7] M. Gharibi, M. Zamani Nejad, and A. Hadi, "Elastic analysis of functionally graded rotating

thick cylindrical pressure vessels with exponentially-varying properties using power series method of Frobenius," *J. Comput. Appl. Mech.*, vol. 48, no. 1, pp. 89–98, 2017, doi: 10.22059/jcamech.2017.233633.143.

[8] M. Zamani Nejad, M. Jabbari, and A. Hadi, "A review of functionally graded thick cylindrical and conical shells," *J. Comput. Appl. Mech.*, vol. 48, no. 2, pp. 357–370, 2017, doi: 10.22059/jcamech.2017.247963.220.

[9] N. J. Pagano and H. J. Hatfield, "Elastic Behavior of Multilayered Bidirectional Composites," *AIAA J.*, vol. 10, no. 7, pp. 931–933, 1972, doi: 10.2514/3.50249.

[10] a J. M. Ferreira, "Analysis of Composite Plates Using a Layerwise Theory and Multiquadrics Discretization," *Mech. Adv. Mater. Struct.*, vol. 12, no. 2, pp. 99–112, 2005, [Online]. Available: http://dx.doi.org/10.1080/15376490490493952.

[11] L. Iurlaro, M. Gherlone, M. Di Sciuva, and A. Tessler, "Refined Zigzag Theory for laminated composite and sandwich plates derived from Reissner's Mixed Variational Theorem," *Compos. Struct.*, vol. 133, pp. 809–817, 2015, doi: 10.1016/j.compstruct.2015.08.004.

[12] E. Reissner, "On the theory of transverse bending of elastic plates," *Int. J. Solids Struct.*, vol. 12, no. 8, pp. 545–554, 1976.

[13] E. Reissner, "A consistent treatment of transverse shear deformations in laminated anisotropic plates," *AIAA J.*, vol. 10, no. 5, pp. 716–718, 1972, doi: http://dx.doi.org/10.2514/3.50194.

[14] E. Reissner, "The effect of transverse shear deformations on the bending of elastic plates," *J. Appl. Mech*, vol. 12, pp. A69–A77, 1945.

[15] R. D. Mindlin, "Influence of Rotatory Inertia and Shear on Flexural Motions of Isotropic, Elastic Plates," *J. Appl. Mech.*, no. 18, pp. 31–38, 1951.

[16] T. N. Nguyen, C. H. Thai, and H. Nguyen-Xuan, "On the general framework of high order shear deformation theories for laminated composite plate structures: A novel unified approach," *Int. J. Mech. Sci.*, vol. 110, pp. 242–255, 2016, doi: 10.1016/j.ijmecsci.2016.01.012.

[17] A. J. M. Ferreira, C. M. C. Roque, and P. a. L. S. Martins, "Analysis of composite plates using higher-order shear deformation theory and a finite point formulation based on the multiquadric radial basis function method," *Compos. Part B Eng.*, vol. 34, no. 7, pp. 627–636, 2003, doi: 10.1016/S1359-8368(03)00083-0.

[18] J.N. Reddy, "Mechanics of laminated composite plates and shells: theory and analysis." CRC Press LLC, Boca Raton, Florida, 2004, doi: 10.1007/978-1-4471-0095-9.

[19] G. Shi, "A new simple third-order shear deformation theory of plates," *Int. J. Solids Struct.*, vol. 44, no. 13, pp. 4399–4417, 2007, doi: 10.1016/j.ijsolstr.2006.11.031.

[20] S. A. Ambartsumian, "On the theory of bending of anisotropic plates and shallow shells," *J. Appl. Math. Mech.*, vol. 24, no. 2, pp. 500–514, Jan. 1960, doi: 10.1016/0021-8928(60)90052-6.

[21] M. Touratier, "An efficient standard plate theory," *Int. J. Eng. Sci.*, vol. 29, no. 8, pp. 901–916, 1991.

[22] M. Karama, K. S. Afaq, and S. Mistou, "A new theory for laminated composite plates," *Proc. Inst. Mech. Eng. Part L J. Mater. Des. Appl.*, vol. 223, no. 2, pp. 53–62, 2009, doi: 10.1243/14644207JMDA189.

[23] M. Aydogdu, "A new shear deformation theory for laminated composite plates," *Compos. Struct. J.*, no. 89, pp. 94–101, 2008.

[24] K. P. Soldatos, "A transverse shear deformation theory for homogeneous monoclinic plates," *Acta Mech.*, vol. 94, no. 3–4, pp. 195–220, 1992.

[25] N. El, A. Tounsi, N. Ziane, I. Mechab, E. Abbes, and A. Bedia, "A new hyperbolic shear deformation theory for buckling and vibration of functionally graded sandwich plate," *Int.*

J. Mech. Sci., vol. 53, no. 4, pp. 237–247, 2011, doi: 10.1016/j.ijmecsci.2011.01.004.

[26] J. Belinha, *Meshless Methods in Biomechanics: Bone Tissue Remodelling Analysis*. Porto: Springer International Publishing, 2014.

[27] J. Belinha, A. L. Araújo, A. J. M. Ferreira, L. M. J. S. Dinis, and R. M. N. Jorge, "The analysis of laminated plates using distinct advanced discretization meshless techniques," *Compos. Struct.*, vol. 143, pp. 165–179, 2016, doi: 10.1016/j.compstruct.2016.02.021.

[28] R. A. Gingold and J. J. Monaghan, "Smoothed particle hydrodynamics: theory and application to non-spherical stars," *Mon. Not. R. Astron. Soc.*, vol. 181, no. 3, pp. 375–389, 1977, doi: 10.1093/mnras/181.3.375.

[29] T. Belytschko, Y. Y. Lu, and L. Gu, "Element-free Galerkin methods," *International Journal for Numerical Methods in Engineering*, vol. 37, no. 2. pp. 229–256, 1994, doi: 10.1002/nme.1620370205.

[30] S. Viana, D. Rodger, and H. Lai, "Overview of meshless methods," *ICS Newsl.*, vol. 14, no. 2, p. 4, 2007, [Online]. Available: http://scholar.google.com/scholar?hl=en&btnG=Search&q=intitle:Overview+of+Meshless+Methods#6.

[31] W. K. Liu, S. Jun, S. Li, J. Adee, and T. Belytschko, "Reproducing kernel particle methods for structural dynamics," *Int. J. Numer. Methods Eng.*, vol. 38, no. 10, pp. 1655–1679, 1995, doi: 10.1002/nme.1620381005.

[32] S. N. Atluri and T. Zhu, "A new Meshless Local Petrov-Galerkin (MLPG) approach in computational mechanics," *Comput. Mech.*, vol. 22, no. 2, pp. 117–127, 1998.

[33] G. R. Liu and Y. T. Gu, "A point interpolation method for two-dimensional solids," *Int. J. Numer. Methods Eng.*, vol. 50, no. 4, pp. 937–951, 2001.

[34] G. R. Liu, "A point assembly method for stress analysis for two-dimensional solids," *Int. J. Solids Struct.*, vol. 39, no. 1, pp. 261–276, 2001.

[35] J. G. Wang and G. R. Liu, "A point interpolation meshless method based on radial basis functions," *Int. J. Numer. Methods Eng.*, vol. 54, no. 11, pp. 1623–1648, 2002.

[36] L. M. J. S. Dinis, R. M. N. Jorge, and J. Belinha, "Analysis of 3D solids using the natural neighbour radial point interpolation method," *Comput. Methods Appl. Mech. Eng.*, vol. 196, no. 13–16, pp. 2009–2028, 2007, doi: 10.1016/j.cma.2006.11.002.

[37] P. Krysl and T. Belytschko, "Analysis of Thin Plates by the Element-Free Galerkin Method," *Comput. Mech.*, vol. 17, no. 1–2, pp. 26–35, 1995.

[38] J. Belinha and L. Dinis, "Analysis of plates and laminates using the element-free Galerkin method," *Comput. Struct.*, vol. 84, no. 22, pp. 1547–1559, 2006.

[39] J. Belinha, "Nonlinear analysis of plates and laminates using the element free Galerkin method," *Compos. Struct.*, vol. 78, no. 3, pp. 337–350, 2007, doi: 10.1016/j.compstruct.2005.10.007.

[40] K. Y. Dai, G. R. Liu, K. M. Lim, and X. L. Chen, "A mesh-free method for static and free vibration analysis of shear deformable laminated composite plates," *J. Sound Vib.*, vol. 269, no. 3–5, pp. 633–652, 2004, doi: 10.1016/S0022-460X(03)00089-0.

[41] B. M. Donning and W. K. Liu, "Meshless methods for shear-deformable beams and plates," *Comput. Methods Appl. Mech. Eng.*, vol. 152, no. 1, pp. 47–71, 1998.

[42] M. Levinson, "An accurate simple theory of the statics and dynamics of elastic plates," *Mech. Res. Commun*, no. 7, pp. 343–350, 1980.

[43] M. Aydogdu, "A new shear deformation theory for laminated composite plates," *Compos. Struct.*, vol. 89, no. 1, pp. 94–101, 2009, doi: 10.1016/j.compstruct.2008.07.008.

[44] S. Xiang, G. Li, W. Zhang, and M. Yang, "A meshless local radial point collocation method for free vibration analysis of laminated composite plates," *Compos. Struct.*, vol. 93, no. 2, pp. 280–286, 2011, doi: 10.1016/j.compstruct.2010.09.018.

[45] A. J. M. Ferreira, "A formulation of the multiquadric radial basis function method for the

analysis of laminated composite plates," *Compos. Struct.*, vol. 59, no. 3, pp. 385–392, 2003.

[46] A. J. M. Ferreira, "Static analysis of functionally graded plates using third-order shear deformation theory and a meshless method," *Compos. Struct.*, vol. 69, no. 4, pp. 449–457, 2005, doi: 10.1016/j.compstruct.2004.08.003.

[47] A. J. M. Ferreira, C. M. C. Roque, R. M. N. Jorge, G. E. Fasshauer, and R. C. Batra, "Analysis of Functionally Graded Plates by a Robust Meshless Method," *Mech. Adv. Mater. Struct.*, vol. 14, no. 8, pp. 577–587, 2007, doi: 10.1080/15376490701672732.

[48] C. Wu and K. Chiu, "RMVT-based meshless collocation and element-free Galerkin methods for the quasi-3D free vibration analysis of multilayered composite and FGM plates," *Compos. Struct.*, vol. 93, no. 5, pp. 1433–1448, 2011, doi: 10.1016/j.compstruct.2010.11.015.

[49] D. F. Gilhooley and M. A. Mccarthy, "Analysis of thick functionally graded plates by using higher-order shear and normal deformable plate theory and MLPG method with radial basis functions," *Compos. Struct.*, vol. 80, no. 4, pp. 539–552, 2007, doi: 10.1016/j.compstruct.2006.07.007.

[50] J. R. Xiao, D. F. Gilhooley, and M. A. Mccarthy, "Analysis of thick composite laminates using a higher-order shear and normal deformable plate theory (HOSNDPT) and a meshless method," *Compos. Part B Eng.*, vol. 39, no. 2, pp. 414–427, 2008, doi: 10.1016/j.compositesb.2006.12.009.

[51] L. M. J. S. Dinis, R. M. Natal Jorge, and J. Belinha, "Analysis of plates and laminates using the natural neighbour radial point interpolation method," *Eng. Anal. Bound. Elem.*, vol. 32, no. 3, pp. 267–279, 2008, doi: 10.1016/j.enganabound.2007.08.006.

[52] J. Belinha, L. M. J. S. Dinis, and R. M. N. Jorge, "The Natural Neighbour Radial Point Interpolation Method: Solid Mechanics and Mechanobiology Applications," *Fac. Eng. da Univ. do Porto*, 2010.

[53] R. L. Hardy, "Theory and applications of the multiquadric-biharmonic method," *Comput. Math. Applic.*, vol. 19, no. 8/9, pp. 163–208, 1990, doi: 10.1017/CBO9781107415324.004.

[54] M. V. V. Murthy, "An improved transverse shear deformation theory for laminated anisotropic plates," *NASA Tech. Pap. 1903*, no. November, 1981.

[55] Z. Kaczkowski, *Plates. In Statical calculations*. Warszawa (in Polish): Arkady, 1968.

[56] V. Panc, *Theories of elastic plates*, 1st ed. Prague: Academia, 1975.

[57] A. Idlbi, M. Karama, and M. Touratier, "Comparison of various laminated plate theories," *Compos. Struct.*, vol. 37, no. 2, pp. 173–184, 1997, [Online]. Available: http://www.sciencedirect.com/science/article/pii/S0263822397800104.

[58] J. L. Mantari, A. S. Oktem, and C. Guedes Soares, "A new higher order shear deformation theory for sandwich and composite laminated plates," *Compos. Part B Eng.*, vol. 43, no. 3, pp. 1489–1499, 2012, doi: 10.1016/j.compositesb.2011.07.017.

[59] X. Wang and G. Shi, "A refined laminated plate theory accounting for the third-order shear deformation and interlaminar transverse stress continuity," *Appl. Math. Model.*, vol. 39, no. 18, pp. 5659–5680, 2015, doi: 10.1016/j.apm.2015.01.030.

[60] D. E. S. Rodrigues, J. Belinha, F. M. A. Pires, L. M. J. S. Dinis, and R. M. N. Jorge, "Homogenization technique for heterogeneous composite materials using meshless methods," *Eng. Anal. Bound. Elem.*, 2018, doi: 10.1016/j.enganabound.2017.12.012.

[61] L. D. C. Ramalho, R. D. S. G. Campilho, J. Belinha, and L. F. M. da Silva, "Static strength prediction of adhesive joints: A review," *Int. J. Adhes. Adhes.*, vol. 96, p. 102451, 2020, doi: https://doi.org/10.1016/j.ijadhadh.2019.102451.